ACS Electrochemistry

Open Access

This article is licensed under CC-BY 4.0

pubs.acs.org/electrochem

Article

The Evolution of Pore Volume during Stripping of Lithium, Sodium, and Potassium Metal Electrodes in Solid-State Batteries

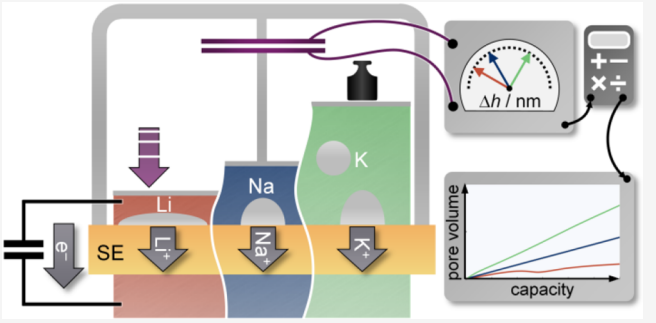
Thomas A. Schall,* Maya Ziegler, Max Wacha, Qianli Ma, Frank Tietz, Janis K. Eckhardt, Chenjie Gan, Aleksandar S. Mijailovic, Brian W. Sheldon, Till Fuchs,* and Jürgen Janek*

Cite This: *ACS Electrochem.* 2026, 2, 2433−2449

Read Online

ACCESS | Metrics & More | Article Recommendations | Supporting Information

ABSTRACT: Alkali metal solid-state batteries (Li, Na, K) suffer from contact loss at the metal|solid electrolyte interface during stripping (discharge), driven by vacancy accumulation and pore formation. This reduces contact area, increases resistance, and promotes dendrite growth during subsequent plating, eventually leading to battery failure. While lithium has been studied extensively, sodium and potassium remain comparatively underexplored despite their high abundance. Their lower yield strength, larger molar volume, and higher homologous temperature strongly affect interfacial contact evolution. Operando electrochemical dilatometry is used to determine the formed pore volume in sodium and potassium metal anodes, enabling evaluation of the vacancy injection ratio (VIR) and comparison with lithium. At low stack pressure, pores form immediately upon stripping for all three metals. The formed pore volume scales with the molar volume across lithium, sodium, and potassium. Increasing current density enhances contact loss and leads to a weaker increase in the formed pore volume in sodium and potassium, with a fraction of the formed pore volume in potassium located inside the metal bulk. In contrast, lithium shows an initial reduction in the formed pore volume (partial pore collapse), followed by a stronger increase at higher current densities. These findings reveal systematic trends among lithium, sodium, and potassium, suggesting lower yield strengths and smaller molar volumes as favorable material properties. Based on these results, a generalized mechanism for pore formation in alkali metal anodes is proposed.



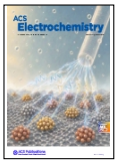
KEYWORDS: *dilatometry, pore formation, lithium metal anode, sodium metal anode, potassium metal anode, alkali metal anode, solid-state battery, vacancy injection ratio*

INTRODUCTION

With advancing technological development and the transition to sustainable energy sources, the demand for energy storage systems is steadily increasing. Alkali solid-state batteries (SSBs) with their respective metal anodes are among the most promising candidates to meet these requirements, as they combine high energy density with enhanced safety compared to conventional lithium-ion batteries.[1−5] Nevertheless, their practical application is still limited by interfacial instabilities that arise during electrochemical cycling. A key limiting process is the loss of contact between the alkali metal anode (AMA) and the solid electrolyte (SE), which originates from pore formation during stripping and limits the cell performance by reducing the accessible capacity and discharge current. Here, we compare pore formation of the lighter three alkali metals, from lithium to potassium to achieve a more general understanding of pore formation as a key factor for cell failure.

During stripping (corresponding to discharge of a cell), pore formation and contact loss can occur at the AMA|SE interface, depending primarily on current density at a given stack pressure.[6,7] Alkali metal atoms are oxidized, and the resulting ions migrate through the SE.[5,8] This ionic charge transfer at the AMA|SE interface generates metal vacancies in the metal at the AMA|SE interface. To preserve interfacial contact, these vacancies must be replenished by atoms from the metal reservoir (e.g., through vacancy diffusion or creep). In the simplest picture, when the local current density surpasses this replenishment limit, vacancies accumulate at the interface, resulting in pore formation. Pore formation is further influenced by adatom diffusion along the pore surface, which proceeds faster than vacancy diffusion in the bulk.[5,8−19] Consequently, the effective

Received: June 3, 2026
Revised: August 10, 2026
Accepted: August 18, 2026
Published: September 8, 2026



Downloaded from pubs.acs.org/aecic7/article-pdf/2/10/2433/6850742/ec-2026-00237p.pdf by KIT BIBLIOTHEK user on 02 November 2026

ACS Publications

© 2026 The Authors. Published by American Chemical Society

https://doi.org/10.1021/acselectrochem.6c00237
ACS Electrochem. 2026, 2, 2433−2449

contact area decreases, leading to local current constriction and eventually to battery failure.[6,7]

In a previous study, we demonstrated that pores form immediately at the onset of stripping in lithium metal anodes on a lithium garnet solid electrolyte ($Li_{6.25}Al_{0.25}La_3Zr_2O_{12}$) at a low applied pressure of about 0.07 MPa, even when these morphological changes remain undetectable by electrochemical impedance spectroscopy (EIS). This observation was enabled by operando electrochemical dilatometry (ECD), which measures height changes of a half-cell with nanometer precision. Unlike operando approaches such as synchrotron X-ray tomography or galvanostatic electrochemical impedance spectroscopy (GEIS), and unlike *post mortem* methods such as focused ion beam scanning electron microscopy (FIB-SEM), operando ECD can detect even the smallest changes in electrode height.[8,9,13,20−28] By comparing the expected homogeneous stripping along the entire interface, as calculated from Faraday's law, with the measured length change, the formed pore volume can be calculated with high sensitivity. This makes ECD uniquely suited for capturing the earliest stages of pore nucleation and growth. Although ECD is a well-established technique,[29−42] a robust methodology for quantitatively determining pore volume from operando height changes has only recently been demonstrated for lithium metal,[43] building on early pioneering experiments on silver electrodes by Majoni and Janek.[10]

Compared to lithium, the heavier alkali metals sodium and potassium are more abundant and potentially less costly. They also have markedly different physical properties that directly affect pore formation. Both metals have a lower yield strength and a higher homologous temperature than lithium, meaning they are mechanically softer and more prone to creep.[44] The larger molar volume of sodium and potassium is expected to affect the accumulation of vacancies and pore evolution during stripping. While homogeneous plating or stripping of lithium with an areal charge of 1 mAh cm^{-2} causes a (Faradaic) length change of 4.85 μm, the same charge causes Faradaic length changes of 8.86 μm and 16.92 μm for sodium and potassium, respectively, suggesting more severe mechanical issues for the heavier alkali metals. These differences in properties provide an opportunity to investigate the influence on pore geometry and pore formation mechanism more systematically. This is particularly relevant as sodium- and potassium-based SSBs are receiving increasing attention as further options beyond lithium SSBs. As their reported critical current densities (CCDs) are higher than those of lithium, it is important to understand how and to what extent pore formation proceeds in sodium and potassium. Furthermore, their distinct material properties are expected to provide a better understanding of the alkali-metal stripping mechanism in general.[17,45−51] We like to add that any practical use of sodium or potassium metal electrodes in full cells will require careful safety considerations; yet this is beyond the scope of this fundamental study.

In this work, we use the high-precision dilatometer setup described earlier[43] to systematically study pore formation dynamics in Na|$Na_{3.4}Zr_2Si_{2.4}P_{0.6}O_{12}$|Na (Na|NZSP|Na) and K|K-β″-Al_2O_3|K (K|KBA|K) symmetric cells (with NZSP and KBA as stable SEs in contact with their parent alkali metals). We then compare the pore formation dynamics in sodium and potassium with previously obtained results for lithium in Li|$Li_{6.25}Al_{0.25}La_3Zr_2O_{12}$|Li (Li|LLZO|Li) cells. By combining lithium data from our previous study with new operando measurements of sodium and potassium, we investigate how key material properties such as yield strength, homologous temperature, and molar volume govern pore formation in AMAs and derive a generalized pore formation mechanism. Ultimately, this study provides unique insights into the fundamental mechanisms of pore formation in AMAs and thus lays the foundation for conceiving strategies to suppress pore formation and to improve the performance of SSBs.

EXPERIMENTAL DETAILS

To quantify operando pore formation and electrode volume changes during alkali metal stripping, an in-house-built dilatometric setup was employed, capable of resolving height variations in the nanometer range under strictly isothermal conditions and constant pressure. The setup has been described in detail in our previous work.[43] The relevant aspects of the measurement setup and experimental conditions are provided below for completeness.

Experimental Conditions for Dilatometric Measurements

All experiments were conducted at low stack pressure (0.07 MPa) and low current densities. At low pressures, pore formation already occurs at low current densities,[43] enabling direct observation of interfacial processes. Under these conditions, height changes can be measured with high accuracy using the high-precision dilatometric setup employed in this work.

Higher stack pressures were deliberately avoided, as they promote creep deformation, particularly in softer alkali metals such as sodium and potassium, thereby interfering with accurate height measurements. In addition, high pressures are impractical for realistic cell designs due to increased mechanical complexity, weight, and cost, partially eliminating the advantages of SSBs.[16]

From a mechanistic perspective, stripping at low pressure with low current densities provides the most fundamental information, as pore formation effects are neither suppressed nor inseparably superimposed with severe creep, which would be the case for higher pressures. Experiments at higher current densities would further require adapted cell designs, such as larger counter electrode areas, and are therefore beyond the scope of the present study.

Operando dilatometric measurements require careful experimental control. Prior to each experiment, the cell was equilibrated under constant load for several days to minimize mechanically induced creep and establish a stable baseline. Mechanical instabilities (e.g., loose components) and unintended electrical effects (e.g., ground loops or parasitic potentials) can introduce artifacts into the displacement signal and were therefore carefully minimized. Each experiment required extensive preparation to ensure reliable and reproducible measurements. Two independently assembled cells were evaluated for each alkali metal, corresponding to one cell at each investigated current density. The Li|LLZO|Li measurements were performed in the previous study reported in ref 43. Given the extensive effort required for each experiment, statistical repeatability could not be assessed. Nevertheless, the clear and internally consistent trends observed across the investigated current densities and alkali-metal systems support the comparative interpretation of the results.

Operando Measurement of Nanometer Scale Height Changes

Height changes of the stripping electrode were monitored using a capacitive push-piston dilatometer, which measures electrode displacement from capacitance changes with nanometer precision.[52−56] A constant mechanical load was applied via weights, while temperature fluctuations were below ±0.01 K in an optimized climate chamber (as discussed below). The electrochemical cell is placed in a friction-free, airtight cell housing.[43] The plating electrode is mechanically decoupled from the measurement axis by placing the alkali metal in a

Downloaded from pubs.acs.org/aecl/c7/article-pdf/2/10/2433/6845074/2/ec-2026-00237p.pdf by KIT BIBLIOTHEK user on 02 November 2026

https://doi.org/10.1021/acselectrochem.6c00237
ACS Electrochem. 2026, 2, 2433−2449

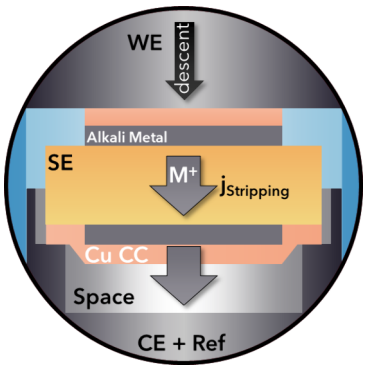


Figure 1. Schematic representation of the mechanical decoupling of the plating side by placement in a recess; adapted from ref 43. Available under a CC-BY 4.0 license. Copyright 2025 Thomas A. Schall et al.

recess, ensuring that only the volume changes of the stripping electrode contribute to the measured height change (Figure 1 – for the full setup see Figure S1). The high accuracy of the measurement setup was demonstrated in ref 43.

Height Change Monitoring

Height change data were measured using two electrochemical push piston dilatometer setups, operated in parallel inside the optimized climate chamber. The two setups differed only in the dilatometric measurement devices used: one setup was equipped with an ElCell ECD-3-nano, the other with an ElCell ECD-4-nano. All other aspects of the setup and measurement conditions were identical. With the ECD-3-nano, the capacitance changes were measured using a PISeca E-852 controller and converted into an analogue signal with a bandwidth of 300 Hz (-10 to +10 V). This analogue signal was converted into a digital signal using an EC-Link AD converter and recorded at 10 Hz using the "El-Cell EC-Link" v 1.3 software (El-Cell GmbH). In the case of the ECD-4-nano, the capacitance changes were measured with a capaNCDT 6200 controller using a median filter (filter width: 7) prior to data transmission. A digital signal is directly generated, recorded and converted into height information with the sensorTOOL 2 software (Micro-Epsilon Messtechnik GmbH & Co. KG) at a frequency of 10.417 Hz. Data processing and visualization were performed using a custom Python script implementing a first-order Butterworth low-pass filter (cut-off = 5×10^{-2} Hz) and subsequent one-second averaging. Table S1 provides the measurement device used for each experiment. The influence of creep is discussed in Supplementary Note 1.

Calculation of the Pore Volume and Vacancy Injection Ratio (VIR)

Operando dilatometry provides direct access to the macroscopic height changes of the stripping electrode, which are used to quantify the volume changes of the electrode during metal dissolution. Pore formation at the AMA|SE interface results in a smaller volume change compared to the value for pore-free stripping. Therefore, by comparing the measured value with that for pore-free stripping, the volume of electrochemically formed pores can be calculated.

Assuming a constant geometric electrode area A, the measured macroscopic volume change ΔV_m can be obtained from the measured displacement of the dilatometer Δh_m according to

$$\Delta V_m = A \cdot \Delta h_m \tag{1}$$

$$\Delta v_m = \frac{\Delta V_m}{A} = \Delta h_m \tag{2}$$

Pore-free stripping involves the uniform removal of all metal atoms that contribute to charge transfer from the interface. Therefore, each atom that is removed contributes to the macroscopic volume change. The height change for uniform stripping Δh_{us} (= Δv_{us}, as area-specific volume change) can be calculated from Faraday's law based on the total charge transferred (Supplementary Note 2 and Eq S1–S8). The difference between the pore-free and measured volume changes corresponds to the electrochemically formed pore volume:

$$\Delta v_p = \frac{\Delta V_p}{A} = \frac{\Delta V_{us} - \Delta V_m}{A} = \Delta v_{us} - \Delta v_m = \Delta h_{us} - \Delta h_m \tag{3}$$

This approach considers a simplified planar electrode geometry. The analysis remains valid for non-ideal interfaces with surface roughness or pre-existing defects, provided the same reference area A is used consistently.[43]

To enable better comparison between different alkali metals, the molar pore volume is used. The molar pore volume gives the pore volume normalized by the molar volume. The molar pore volume Δv_p^{mol} can be calculated from the formed pore volume Δv_p using the molar volume V_{mol} of the respective metal, normalizing the intrinsic atomic packing density of each metal.

$$\Delta v_p^{mol} = \frac{\Delta v_p}{V_{mol}} \tag{4}$$

The vacancy injection ratio (VIR) is used to quantify the balance between vacancy generation and compensation at any given point during stripping. The VIR expresses the fraction of unfilled metal vacancies generated during stripping at each point. The concept of the VIR was introduced in ref 43. In this study, a differential calculation of the VIR, based on the deviation of the measured height-change rate from that expected for uniform stripping, is used and is defined as:

$$\mathrm{VIR} = 1 - \left(\frac{dv_m}{dt}\right) \Big/ \left(\frac{dv_{us}}{dt}\right) = 1 - \left(\frac{dh_m}{dt}\right) \Big/ \left(\frac{\Delta h_{us}}{\Delta t}\right) \tag{5}$$

In contrast to the cumulative VIR definition used in ref 43, the VIR shown here reflects the instantaneous value at each plotted capacity point rather than the cumulative average from the beginning of stripping. Throughout this work, VIR refers to this differential quantity. A VIR of 0 corresponds to fully compensated vacancy formation (*i.e.*, no pore formation), while higher VIR values indicate a larger fraction of unfilled vacancies and consequently more pronounced pore formation. A VIR below zero corresponds to pore refilling, *i.e.*, pore collapse.

Optimized Climate Chamber

Measurements were conducted in an optimized climate chamber (BINDER KB ECO 240), which is equipped with an additional internal insulation box (~80 L) to ensure thermal stability better than 10^{-2} K. The chamber employs vibration-free Peltier cooling, and mechanical disturbances were minimized by mounting the chamber on cork damping mats (22 mm thickness). All measurements were performed in a windowless, low-vibration laboratory without exterior walls and restricted access during measurements.

Electrochemical Characterization

Electrochemical cycling and impedance spectroscopy were performed using a Bio-Logic SP-300 potentiostat with EC-Lab V.11 software. The stripping electrode was connected to the working electrode, and the plating side to the counter and reference electrodes. Galvanostatic electrochemical impedance spectroscopy (GEIS) was conducted between 7 MHz and 1 Hz, with an amplitude equivalent to 10 % of the applied DC current density. The impedance data were analyzed using the RelaxIS 3 software. The *Kramers–Kronig test* was used to identify and remove low-quality data. Subsequently,

Downloaded from pubs.acs.org/aecic7/article-pdf/2/10/2433/6850742/ec-2026-00237p.pdf by KIT BIBLIOTHEK user on 02 November 2026

https://doi.org/10.1021/acselectrochem.6c00237
ACS Electrochem. 2026, 2, 2433−2449

Distribution of Relaxation Times (DRT) data were calculated from the real part of the impedance data. In the Tikhonov regularization problem, the second derivative of the distribution function $\gamma(\tau)$ was used. The regularization parameter $\lambda = 10^{-3}$ was used in the calculations. Based on these DRT data, contour plots were created, as previously described in ref 43. For selected spectra see Figure S2.

Temperature Monitoring

The temperature was continuously monitored using four Pt-100 thermocouples, which were placed at critical points of the ECD-4 measurement setup (press cell casing, two at the measurement unit, and climate chamber). Data were recorded via a Keithley 2700 multimeter and 7700 multiplexer. Measurements were only initiated once temperature variations remained within ±0.01 K for 30 minutes. As both setups were located within the insulation box inside the climate chamber, the same temperature was assumed for both setups. The exact temperature for each experiment is provided in Table S1.

Preparation of the Electrochemical Cells

Lithium Metal-Based Cells. The lithium-based symmetric cells and all the experimental data used in this study are identical to those previously reported in ref 43. No new measurements were conducted for the lithium system. Instead, the original operando data were analyzed in the context of the present comparative study with sodium and potassium. For completeness, the assembly of Li|LLZO|Li cells is provided in Supplementary Note 3.

Sodium Metal-Based Cells. The sodium-based symmetric cells were prepared using a Na|NZSP|Na cell configuration. The NZSP ($Na_{3.4}Zr_2Si_{2.4}P_{0.6}O_{12}$) solid electrolyte was synthesized via a solution-assisted solid-state reaction (SA-SSR) route, following the procedure described in ref 57. After sintering green bodies with Ø 10 mm, the resulting NZSP pellets exhibited a relative density above 95% with Ø ∼8 mm and d ∼1.5 mm.

Both sides of the NZSP pellets were used with their as-sintered surfaces. Sodium electrodes (Ø 5 mm) were used on both sides of the unpolished NZSP pellet. Before attaching the electrodes to the SE, the passivation layer was mechanically removed from the SE-facing side of each sodium electrode by scratching with a ceramic knife. A copper foil (20 μm thickness) with Ø 8 mm was used on both sides as current collectors. The electrodes were then attached to the NZSP pellet and uniaxially pressed at 8 MPa for 1 minute in an in-house-built pressure setup previously reported by Krauskopf *et al.*,[8] followed by isostatic pressing at 133 MPa for 15 minutes, in accordance with previously established protocols.[58] Isostatic pressing of sodium electrodes was found to generate a negligible interface-related contribution (∼1 Ω cm^2) resulting in ideal sodium electrodes (Na_{id}).[8,58] After pressing, the sodium electrodes had a Ø ∼6 mm and d ∼100 μm. Subsequently, the assembled cells were heated to 95 °C for 15 h in argon atmosphere. All preparation steps were carried out entirely in an argon atmosphere (MBraun, $p(H_2O)/p < 1.0$ ppm, $p(O_2)/p < 0.1$ ppm).

Potassium Metal-Based Cells. The potassium-based symmetric cells were prepared using K-β″-Al_2O_3 (KBA) SE. The KBA pellets (Ø 10 mm) were obtained from Ionotec Ltd., UK. According to the manufacturer, these pellets are produced by ion exchange from Na-β″-Al_2O_3, yielding a degree of potassium exchange of > 90 %.

Prior to cell assembly, the pellet surfaces were mechanically polished with SiC P400, P1000 and finally with P1500 abrasive paper frequently changing the polishing direction to prevent preferential polish orientation. Subsequently, the pellets were heat-treated at 875 °C for 4 h in dry argon atmosphere according to ref 48.

Potassium electrodes were prepared from potassium chunks stored under heptane. The metal was cut with a knife and the surface degradation layer was removed by scratching. The cleaned metal was then rolled into thin foils, from which discs with a Ø 6 mm were punched. The potassium discs were placed as electrodes on both sides of the KBA pellet together with copper current collectors with a diameter of 9.6 mm (20 μm thickness). The assembled cells were subsequently isostatically pressed at 200 MPa for 30 min.

To minimize possible interferences from residual sodium in the K-β″-Al_2O_3 lattice, each assembled K|KBA|K cell was first cycled once. After this initial activation, the electrodes were removed, and the steps described above were repeated. All preparation and assembly steps were conducted entirely in an argon-filled glovebox (MBraun, $p(H_2O)/p < 1.0$ ppm, $p(O_2)/p < 0.1$ ppm).

Microscopic Imaging and Digital Image Analysis. A Leica EMSPIRA-3 optical microscope in an argon-filled glovebox (MBraun) was used for optical imaging.

The exact anode area was measured using the open-source software Fiji. Images from the Leica EMSPIRA-3 optical microscope were imported using the Bio-Formats plugin, which reads the scale information from the EXIF data of the microscope image. The area was manually selected using the 'oval selection' tool for lithium and sodium cells and using the "polygon selection" tool for potassium and then measured. As the anodes deform when inserted into the press cell and the measuring pressure is applied, determining the exact anode area is slightly prone to error.

Focused Ion Beam Scanning Electron Microscopy (FIB-SEM). Using a XEIA3 dual-beam FIB-SEM system (TESCAN GmbH, Czech Republic), cross-sections of the peeled-off anodes were prepared and analyzed. Sample transfer from the argon-filled glovebox to the microscope chamber was carried out in inert-gas conditions using a Leica EM VCT500 vacuum transfer shuttle (Leica Microsystems GmbH, Germany).

Ion milling was performed at temperatures below −120 °C to minimize degradation of the alkali metals through heating caused by milling. The electrodes were placed on a 20° holder with the current collector facing the ion beam and polished using Xe^+ ions at 30 kV, with beam currents of 1300–700 nA. The current collector of the Li electrode was glued onto sticky copper tape and placed further onto a steel disc as this reduces curtaining and rippling during ion milling. Only the sodium electrode was further polished down with a beam current of 300 nA to reduce curtaining. Imaging of the prepared cross-sections was performed using an in-beam secondary electron detector in analytic and high-resolution mode at 4 kV.

Finite-Element Simulations. Finite-element simulations were performed in Abaqus/Standard 2020 (Dassault Systèmes) to quantify how interfacial pore geometry influences stress concentration at an AMA|SE. The FEM analysis was conducted for the perfectly bonded (no-slip) interfacial condition shown in Figure 9b. The limiting case of frictionless contact was evaluated analytically, as described below. A mesh-refinement check for the numerical simulations is provided in Figure S3 and discussed in the Supplementary Note 4.

The model was defined as axisymmetric, such that the interfacial pore corresponds to an axisymmetric cavity at an AMA|SE interface. The sodium electrode was modeled as a linear elastic solid with Young's modulus $E = 4.6$ GPa and Poisson's ratio $\nu = 0.41$.[46] A tie constraint (bonded contact) was applied at the Na|SE interface to enforce displacement continuity to represent a perfectly bonded interfacial condition, whereas an axisymmetric boundary condition was applied to represent the frictionless contact condition. A uniform far-field compressive stack pressure of 0.07 MPa was applied to represent the experimentally relevant loading condition.

The domain was discretized using approximately 90,000 axisymmetric four-node bilinear reduced-integration elements (CAX4R). The mesh was locally refined near the pore edge to a minimum element size of 0.1 μm to better resolve the strong stress gradients at the pore tip. For bonded interfaces between dissimilar elastic materials, the stress field near an interfacial crack/tip (and more generally near certain interface-edge/corner configurations) can exhibit singular behavior, meaning that the pointwise peak stress predicted by FEM may continue to increase with mesh refinement rather than converging to a finite "true maximum", as shown in the mesh-refinement study in Figure S3 and discussed in the Supplementary Note 4. The bonded interfacial void problem may exhibit a singular near-edge stress field, such that the pointwise peak stress does

Downloaded from pubs.acs.org/aeclc7/article-pdf/2/10/2433/6845074/2/ec-2026-00237p.pdf by KIT BIBLIOTHEK user on 02 November 2026

https://doi.org/10.1021/acselectrochem.6c00237
ACS Electrochem. 2026, 2, 2433−2449

not necessarily converge to a finite value with mesh refinement. The FEM results should therefore be interpreted as representing the upper limiting case of interfacial constraint rather than a literal prediction of a finite edge stress. Owing to computational limitations, the pore geometry was parameterized over a finite range of a and b values, corresponding to the black dashed region in Figure 9c.

An analytical solution was used to quantify the effect of interfacial pore geometry on stress concentration for the shear-free (frictionless-slip) interfacial condition, following refs 59,60. In this limiting case, the interface transmits no shear traction and the stress concentration at the pore edge can be described by a closed-form expression. The maximum in-plane normal stress at the pore edge is written as

$$\sigma_{zz}^{max} = C_z \sigma_\infty \tag{6}$$

where σ_∞ is the far-field applied stacking pressure and C_z is the stress concentration coefficient. For a pore characterized by half-length a (along the interface) and half-height b (normal to the interface), the aspect-ratio parameter is defined as

$$\beta = \frac{a}{b} \tag{7}$$

The coefficient C_z is then given by

$$C_z = \frac{1-\nu-(1.5-\nu)\beta^2 + 2\beta^4 + [\nu-(1.5+\nu)\beta^2]\beta^2 Q'}{N'} \tag{8}$$

with

$$N' = 1+\beta^2-\nu-[2-\beta^2-2\nu+(1+\nu)\beta^2 Q']\beta^2 Q' \tag{9}$$

and

$$Q' = -\frac{1}{2\sqrt{1-\beta^2}} \ln\left(\frac{1-\sqrt{1-\beta^2}}{1+\sqrt{1-\beta^2}}\right) \tag{10}$$

Here, ν is the Poisson's ratio of the metal electrode.

RESULTS AND DISCUSSION

In this section, operando measurements of pore formation in symmetric cells with sodium and potassium metal anodes are presented using the high-precision dilatometric setup described in ref 43. The height change of the symmetric cell is measured by ECD with nanometer-scale accuracy (as demonstrated in ref 43). To isolate the stripping process, the plating electrode is placed in a recess, ensuring that only the height change of the stripping side is detected.

The corresponding formed pore volume and vacancy injection ratio (VIR) are calculated from the measured height change by comparison with the theoretical (Faradaic) height change for uniform stripping. Further details on the measurement setup and data analysis are provided in the **Experimental Details** section under **Operando Measurement of Nanometer Scale Height Changes.**

All measurements were performed at a constant stack pressure of 0.07 MPa and at 25 °C to focus on fundamental pore formation processes under well-controlled conditions. At low pressures, pore formation occurs already at low current densities, while higher pressures would enhance creep deformation and complicate interpretation of the height changes. Due to the high sensitivity of the dilatometric measurements, particular care was taken to ensure mechanical and electrical stability (see **Operando Measurement of Nanometer Scale Height Changes** for details).

Pore formation during stripping is characterized by three complementary quantities: the formed pore volume, which reflects the extent of pore formation; the VIR, which quantifies the fraction of vacancies that are not refilled during stripping; and the cell resistance, which indicates changes in interfacial contact. Before stripping, pores are assumed to be absent in all cells, as the alkali metal electrodes were isostatically pressed to the SE at stresses well above the yield strength. This corresponds to an initial state with full interfacial contact.

The results are first separately presented for sodium and potassium metal anodes to establish the individual pore formation behavior. Subsequently, pore formation in lithium,[43] sodium, and potassium is directly compared to identify systematic trends among the alkali metals. Based on these observations, a generalized pore formation mechanism is developed that explains the observed differences in pore evolution, including the reduced pore volume growth at higher current densities and the material-dependent behavior. This mechanistic interpretation is supported by a combined analytical and finite element analysis of the stress distribution at interfacial pores. Finally, the implications for AMAs are discussed.

Stripping of Sodium Metal Anodes

In the symmetric Na|NZSP|Na cells, the sodium electrode monitored by dilatometry was stripped at current densities of 100 and 200 μA cm^{-2}, and the corresponding data are shown up to an areal capacity of 5 mAh cm^{-2} (*i.e.*, amount of sodium) in Figure 2. The evolution of the pore volume and the corresponding DC resistance *vs.* areal capacity are displayed in Figure 2a. Interpretation of the results for later stages during stripping is difficult; see Supplementary Note 5, Figures S4 and S5 for details. The measured height change is shown in Figure S6. Initially, the formed pore volume increases more steeply for both current densities, with slightly different initial slopes. At higher capacities, both curves converge to an equal slope. Up to ~2 mAh cm^{-2}, the capacity-dependent evolution is nearly identical, indicating a regime independent of current density. A regime is considered current-density-independent

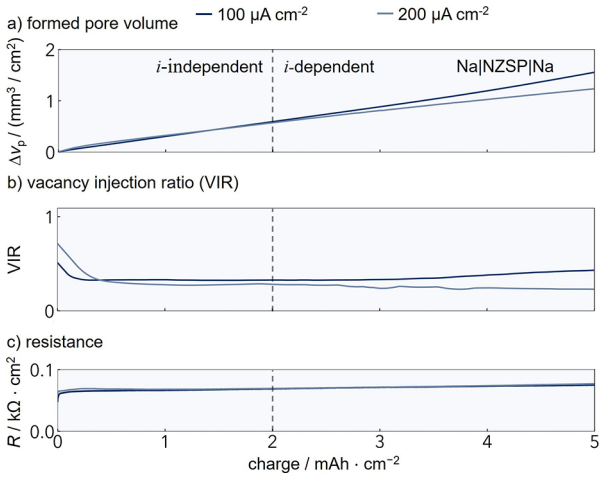


Figure 2. Stripping of sodium metal anodes at 100 and 200 μA cm^{-2} up to 5 mAh cm^{-2}. (a) Formed pore volume, (b) VIR, and (c) cell resistance.

Downloaded from pubs.acs.org/aecl/c7/article-pdf/2/10/2433/6845074/2/ec-2026-00237p.pdf by KIT BIBLIOTHEK user on 02 November 2026

https://doi.org/10.1021/acselectrochem.6c00237
ACS Electrochem. 2026, 2, 2433−2449

when the curves obtained at different current densities show the same capacity-dependent evolution within experimental uncertainty.

For capacities above ~2 mAh cm^{-2}, the formed pore volume at 200 μA cm^{-2} is smaller than that at 100 μA cm^{-2}, which appears counter-intuitive at first and is discussed in detail in section **Pore Formation Mechanism for Alkali Metals**. This indicates that current density influences pore evolution beyond simple scaling with stripping rate. Here, pores are assumed to form exclusively at the AMA|SE, as no evidence of bulk pores is observed in *post mortem* FIB-SEM analyses (Figure S7 and ref 58).

The analysis of the VIR (Figure 2b) clarifies these results. At the onset of stripping, the VIR is relatively high but decreases to nearly identical values for both current densities up to 2 mAh cm^{-2}. At higher capacities, the VIR increases for 100 μA cm^{-2} while decreasing for 200 μA cm^{-2}. This similarity suggests rapid pore nucleation at the beginning of stripping, followed by a quasi-stationary regime. Beyond this capacity, a transition occurs: the VIR decreases for 200 μA cm^{-2}, while it increases for 100 μA cm^{-2}. Apparently, additional factors beyond current density influence pore evolution.

Throughout the investigated capacity range, the cell resistance (including interface (*i.e.*, constriction), grain boundary and bulk contributions) remains low (Figure 2c), and no evidence of constriction is observed in the distribution of relaxation times (DRT) data (Figure S8).[43] This suggests that substantial interfacial contact is maintained, as constriction effects typically become apparent below a remaining contact area of approximately 50%.[26] At a capacity of 5 mAh cm^{-2}, the total pore volume reaches 1.6 mm^3 cm^{-2} for 100 μA cm^{-2} and 1.2 mm^3 cm^{-2} for 200 μA cm^{-2}. Assuming a remaining contact area of 50 % and a cylindrical pore shape, this corresponds to average pore depths of approximately 32 μm and 24 μm, respectively (Supplementary Note 6 and Eq S9–S11). Assuming a higher remaining contact area fraction would correspond to deeper pores.

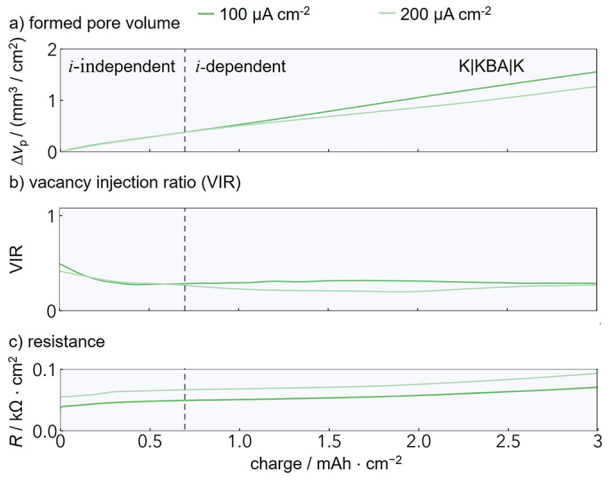


Figure 3. Stripping of potassium metal anodes at 100 and 200 μA cm^{-2} up to 3 mAh cm^{-2}. (a) Formed pore volume, (b) VIR, and (c) cell resistance.

Stripping of Potassium Metal Anodes

To investigate pore formation in potassium metal anodes, symmetric K|KBA|K cells were examined with current densities of 100 and 200 μA cm^{-2}. This is shown in Figure 3 up to 3 mAh cm^{-2}, which corresponds to roughly the same stripped metal volume as in the sodium case. For higher areal capacities, the reliability of the results cannot be guaranteed due to deformation of the current collector (see Supplementary Note 7, Figures S9 and S10).

The evolution of the formed pore volume *vs.* the stripped charge (*i.e.*, amount of potassium) is shown in Figure 3a. The directly measured height signal is provided in Figure S11. During the early stripping stage (< 0.2 mAh cm^{-2}), the slope is steeper for both current densities but converges to an equal slope at higher capacities. Up to a capacity of ~1 mAh cm^{-2}, both curves show the same capacity-dependent evolution within experimental uncertainty, marking a regime that is independent of current density.

At higher capacities, the formed pore volume grows faster at 100 μA cm^{-2} than at 200 μA cm^{-2}. At 3 mAh cm^{-2}, the formed pore volumes correspond to 1.5 mm^3 cm^{-2} for 100 μA cm^{-2} and 1.3 mm^3 cm^{-2} for 200 μA cm^{-2}, respectively. Post-mortem FIB-SEM analysis of the potassium anode stripped at 200 μA cm^{-2} reveals the presence of pores within the metal bulk (Figure S12). Consequently, the measured pore volume in potassium cannot be assigned exclusively to interfacial pores.

The corresponding VIR (Figure 3b) provides further insight into the pore-formation dynamics. Initially, VIR values are elevated and decrease to similar values for both current densities up to 0.7 mAh cm^{-2}. The VIR is calculated from the differential height signal (Eq 5) and is therefore more sensitive to changes than the formed pore volume. Beyond this capacity, the VIR diverges slightly: for 100 μA cm^{-2}, the VIR increases, whereas it decreases for 200 μA cm^{-2}, before both approach similar values again starting from ~2 mAh cm^{-2}. Accordingly, 0.7 mAh cm^{-2} is taken as the upper limit of the current-density-independent regime for potassium.

Throughout stripping, the cell resistance remains low and stable (Figure 3c), and no evidence of constriction is observed in the DRT data (Figure S13), indicating that substantial interfacial contact is maintained, as constriction effects typically become apparent for remaining contact areas below ~50%.[26]

No evidence of pore collapse or re-established contact is observed within the investigated capacity range. Overall, the evolution of pore volume and VIR in potassium follows trends similar to those observed for sodium, while also exhibiting distinct differences that will be discussed in the following section.

Comparison of Pore Formation in Lithium, Sodium, and Potassium Anodes

The obtained results with sodium and potassium electrodes exhibit very similar qualitative trends, as already evident from the individual analyses above. In this section, the stripping behavior of lithium, sodium, and potassium is directly compared. The lithium stripping behavior is only briefly summarized here as a reference, as it has been discussed in detail in our previous work,[43] from which the lithium data used for comparison were also taken. Based on the S-shaped resistance profile for lithium stripping, three distinct regimes of pore formation were identified.[43] In **Regime I** the formed pore volume is independent of current density, and the resistance

Downloaded from pubs.acs.org/aecic7/article-pdf/2/10/2433/6845074/2/ec-2026-00237p.pdf by KIT BIBLIOTHEK user on 02 November 2026

https://doi.org/10.1021/acselectrochem.6c00237
ACS Electrochem. 2026, 2, 2433−2449

remains low. Pore nucleation immediately starts at the onset of stripping. **Regime II** is characterized by a pronounced step in the resistance profile, accompanied by a reduction in pore volume. This partial pore collapse refers to a single reduction in pore volume. As pore collapse begins, a clear constriction signal is detected for lithium, which causes the pronounced increase in resistance. Although the resistance increase and the decrease in pore volume occur at the same capacity, they reflect two separate processes: contact constriction and partial pore collapse, respectively. In **Regime III** the contact area stabilizes. In this regime, the total pore volume at 200 μA cm^{-2} is approximately twice that observed at 100 μA cm^{-2} at the same capacity.

A direct comparison of lithium, sodium, and potassium stripping at 0.07 MPa and 25 °C is shown in Figure 4. At 100 μA cm^{-2} (Figure 4a, left), the formed pore volume increases systematically from lithium to sodium to potassium. Sodium exhibits approximately twice, and potassium approximately four times the pore volume of lithium, consistent with their respective molar volumes: sodium (V_m(Na) = 2.4·10^{-5} m^3 mol^{-1}) and potassium (V_m(K) = 4.5·10^{-5} m^3 mol^{-1}) exhibit approximately two- and four-fold higher molar volumes than lithium (V_m(Li) = 1.3·10^{-5} m^3 mol^{-1}) [61–63] (Supplementary Note 8 and Eq S12–S15). For 200 μA cm^{-2} (Figure 4a, right), this relationship persists up to a stripped capacity of approximately 0.6 mAh cm^{-2} (**Regime I** for lithium in ref 43), while the formed pore volume is independent of current density for all three metals. For higher capacities (**Regime II** for lithium in ref 43, 0.6 to 2 mAh cm^{-2}) the pores in lithium (partially) collapse, as indicated by a decrease in pore volume. At 100 μA cm^{-2}, the pore volume of lithium slowly increases again after the pore collapse and approaches the values at lower capacities. At 200 μA cm^{-2}, the pore volume increases more strongly after the collapse, eventually reaching values comparable to those observed for sodium.

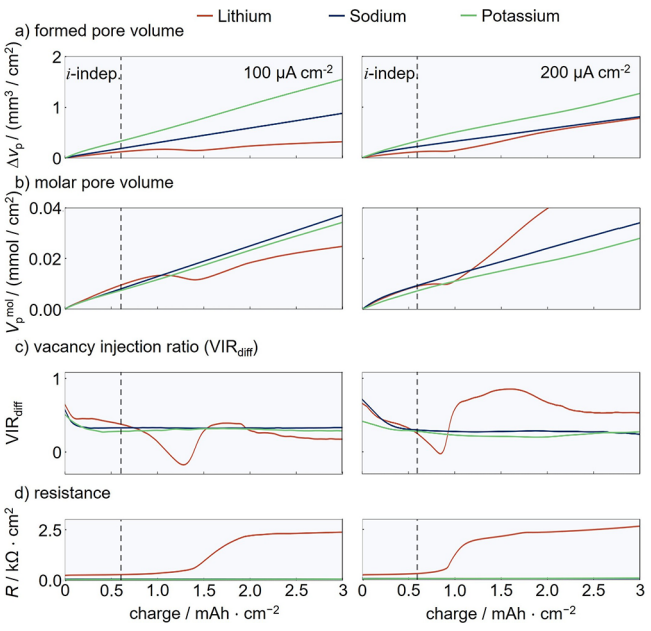


Figure 4. Comparison of Li, Na, and K metal anodes during stripping at (left) 100 μA cm^{-2} and (right) 200 μA cm^{-2}. (a) Formed pore volume, (b) molar pore volume, (c) VIR, and (d) cell resistance. The early regime is independent of current density for Li, Na, and K. Li data are taken from ref 43. Available under a CC-BY 4.0 license. Copyright 2025 Thomas A. Schall et al.

To further analyze these results, Figure 4b shows the molar pore volume. The molar pore volumes of sodium and potassium are nearly identical for the same current density. Lithium deviates for 100 μA cm^{-2} only in the range of pore collapse (**Regime II**). Here, collapse causes a transient decrease in molar pore volume, followed by continued growth with a similar slope as before collapse. At 200 μA cm^{-2}, lithium likewise shows a transient decrease during collapse; however, the subsequent growth is markedly steeper, resulting in an approximately two-fold higher molar pore volume compared to the regime before collapse.

The VIR is compared in Figure 4c. At low capacities, the VIR is very similar for all three alkali metals (~40 %) and independent of current density (**Regime I** for lithium). Beyond this range, the VIRs of sodium and potassium begin to deviate slightly depending on current density, while remaining within a relatively narrow range. In contrast, lithium exhibits a distinctly different behavior. In **Regime II**, the VIR decreases significantly at both current densities. At 100 μA cm^{-2}, the VIR drops below zero, thereby decreasing the pore volume, before increasing again towards values similar to sodium and potassium. At 200 μA cm^{-2}, the VIR also shows a pronounced decrease followed by a strong increase to values significantly exceeding those of sodium and potassium. Notably, lithium shows faster pore volume growth at higher current densities, whereas sodium and potassium exhibit the opposite trend, with a weaker increase in formed pore volume at higher current densities. Therefore, the VIR results are in good accordance with the molar pore volume, which remains nearly identical for all three alkali metals within the capacity range prior to pore collapse in lithium, suggesting similar steady-state behavior for all three alkali metals as discussed in the following section. The onset of current-density-independent behavior differs significantly between the AMAs and is indicated in the VIR curves by the first divergence between the two current densities. This occurs at ~0.6 mAh cm^{-2} for lithium, ~2 mAh cm^{-2} for sodium, and ~0.7 mAh cm^{-2} for potassium.

The resistance during stripping is plotted in Figure 4d. For both current densities, the resistances of sodium and potassium electrodes remain low and comparable throughout the analyzed range, and DRT analyses do not show signs of constriction (Figures S8 and S13). In contrast, during stripping of lithium, the resistance increases significantly due to contact constriction,[43] indicating that stripping capacity is clearly limited under these conditions. The absence of detectable constriction effects in sodium and potassium indicates a higher remaining contact area compared to lithium. Together with the significantly increased pore volume for sodium and potassium compared to lithium, pores in sodium and especially potassium are, on average, substantially deeper than in lithium. A pore collapse is observed only for lithium, whereas no evidence of pore collapse is found for sodium and potassium under the investigated conditions, highlighting a fundamental difference in pore evolution among the alkali metals for higher capacities. Importantly, at low capacities (<0.6 mAh cm^{-2}), no corresponding increase in resistance and no signs of constriction effects are observed, while pore formation is already evident for all three alkali metals (see Figure 4a,d). This shows that pore formation initiates prior to the onset of measurable constriction effects.

To qualitatively compare the late-stage pore morphologies, *post mortem* FIB-SEM cross-sections and top-view SEM images

Downloaded from pubs.acs.org/aecic7/article-pdf/2/10/2433/6850742/ec-2026-00237p.pdf by KIT BIBLIOTHEK user on 02 November 2026

https://doi.org/10.1021/acselectrochem.6c00237
ACS Electrochem. 2026, 2, 2433−2449

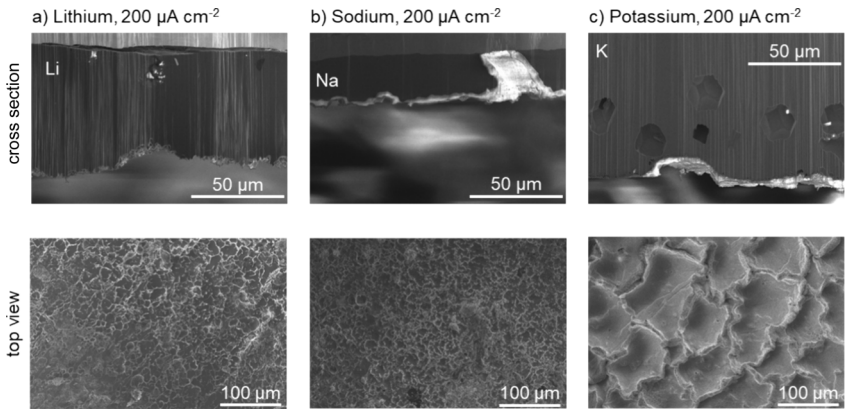


Figure 5. Post mortem FIB-SEM (top row) and top-view SEM analyses (bottom row) of anodes peeled from the SE after stripping and practically complete contact loss at 200 µA cm^{-2}. (a) Lithium anode after stripping of 21.3 mAh cm^{-2}; (b) sodium anode after stripping of 8.7 mAh cm^{-2}; and (c) potassium anode after stripping of 4.2 mAh cm^{-2}.

were obtained from peeled-off samples stripped at 200 µA cm^{-2} (Figure 5). The total stripped capacities after practically complete contact loss differ between samples (Li: 21.3 mAh cm^{-2}; Na: 8.7 mAh cm^{-2}; K: 4.2 mAh cm^{-2}). Moreover, these images represent advanced stripping states and do not provide direct evidence of the pore dimensions or their evolution during the earlier stages analyzed by operando dilatometry. Therefore, a quantitative comparison of absolute pore volume or mean pore height is not meaningful. At these advanced *post mortem* states, lithium exhibits a fine distribution of predominantly shallow pores with only a limited number of deeper pores, while sodium shows fewer and deeper pores in the cross section. In top-view the pore morphologies of lithium and sodium appear visually similar.

For potassium, a layered pore structure is visible at the interface, extending partially into the bulk of the metal. The top-view image further shows that individual potassium pores occupy comparatively large lateral areas, even though a substantial fraction of the total porosity resides in the bulk. Based on a rough geometric estimate from Figure S12, ~40% of the pore volume at this advanced stripping state is located at the interface, while the remaining 60 % contribute to bulk pores within the metal. Given that the total pore volume in potassium is roughly twice that of sodium under the analyzed conditions, this estimate implies that the interfacial pore volume of potassium is comparable to that of sodium. Moreover, the hexagonal cavities in potassium and a clear three-dimensional morphology appear consistent with the expected Wulff construction of pores within the surrounding body-centered cubic potassium crystals, suggesting that the pores approach a thermodynamic equilibrium shape within the bulk. This observation points to fast atomic diffusion in potassium at room temperature. In contrast, no bulk pores were detected in lithium and sodium. The *post mortem* analyses in Figure 5 must be interpreted in the context of the operando electrochemical data. In the capacity range analyzed by dilatometry, neither sodium nor potassium showed detectable constriction signatures, implying that the remaining contact area during the measurement was still comparatively high (> ~50%[26]) and thus larger than at the time of peeling, which occurred after near-complete contact loss. Moreover, for potassium, fast diffusion kinetics and concentration gradients may drive further pore growth in the bulk even after stripping is stopped. Accordingly, the cross-sections and top-views primarily provide qualitative information on the type of the late-stage pore morphologies, whereas quantitative conclusions regarding pore dimensions during the operando measurements remain uncertain. The observed stripping behavior for sodium and potassium is in good agreement with literature reports; a detailed comparison is provided in Supplementary Note 9.

Pore Formation Mechanism for Alkali Metals

Based on the comparative analysis of lithium, sodium, and potassium, the observed differences in pore evolution can be rationalized within a unified mechanistic framework. While all three alkali metals exhibit similar pore formation behavior at low capacities, their subsequent evolution diverges significantly with increasing capacity, particularly with respect to pore geometry, current-density dependence, and the occurrence of pore collapse or bulk pores. In the following, the underlying processes governing pore formation and evolution are discussed to establish a generalized mechanism for alkali metal anodes.

Mechanistic Factors Governing Pore Evolution. At the beginning of stripping, the VIR is elevated for all three alkali metals (Figure 4c). This initial increase indicates that stripping proceeds preferentially at specific sites at the interface. Possible reasons are microstructural effects, morphological irregularities and impurities. As stripping proceeds, the VIR decreases and approaches a stable and almost identical value for lithium, sodium and potassium, suggesting similar behavior and mechanisms for all three alkali metals despite the large differences in material properties. However, the transition from the initial current-density-independent to a current density-dependent regime occurs at different capacities for the three alkali metals (Li: ~0.6 mAh cm^{-2}; Na: ~2 mAh cm^{-2}; K: ~0.7 mAh cm^{-2}). This indicates that pore evolution differs between the alkali metals, resulting in differences in pore geometry, particularly in the lateral extent and effective contact area.

Beyond the material-dependent differences discussed above, the influence of current density on pore evolution must also be considered. Figures 2 and 3 show that higher current densities lead to a lower formed pore volume at higher capacities. The observed differences suggest that the current density may

Downloaded from pubs.acs.org/aecic7/article-pdf/2/10/2433/6845074/2/ec-2026-00237p.pdf by KIT BIBLIOTHEK user on 02 November 2026

https://doi.org/10.1021/acselectrochem.6c00237
ACS Electrochem. 2026, 2, 2433−2449

influence pore shapes, which cannot be measured in a 1D dilatometric measurement, thereby altering the stress distribution and the resulting creep rate. Note that different pore geometries can show the same pore volume (Figure 6a) but alter the stress distribution in the surrounding metal, with increasing pore area leading to higher stresses at the interface. With increasing local pressure, the creep rate increases accordingly, which counteracts further pore growth. Consequently, pore volume growth is expected to be slower for flat, laterally extended pores than for narrow, deep pores. This consideration reflects the total interfacial area covered by pores and is independent of the absolute number of pores, although the latter is expected to increase with current density according to nucleation theory.[9]

Assuming that higher current densities promote a larger area covered with pores ("flat pores"), the experimentally observed lower pore volume at 200 μA cm^{-2} can be explained by enhanced creep rates slowing down further pore growth. This evolution is summarized schematically in Figure 6b,c. Even in the initial regime, where the total pore volume is nearly identical for both current densities, differences in pore geometry are expected, which become more pronounced with increasing capacity. The progressive reduction of the remaining contact area in the case of flatter pores leads to increasing local stresses and enhanced creep deformation. At higher capacities, this results in a measurably smaller pore volume at higher current densities. We emphasize that, with respect to constriction effects and cell failure, the pore area and the resulting loss of interfacial contact are more critical than the absolute pore volume.

Pore nucleation determines the distance between neighboring pores and may therefore affect their subsequent evolution. Small pore distances can promote progressive coalescence during stripping which can lead to delamination before the anode develops a pore geometry that triggers a distinct, measurable collapse.[64,65] The number and distance of pores cannot be determined by dilatometry. For lithium, the observed decrease in pore volume shows that pore collapse occurs under the present conditions. A higher number of pores at 200 μA cm^{-2} may nevertheless contribute to earlier coalescence and contact loss. For sodium and potassium, pronounced coalescence and delamination are unlikely within the analyzed capacity range, as the remaining contact area is likely above ~50% because no constriction signal is observed.

The origin of this geometry change can be understood from the kinetics of vacancy transport. Pore formation is diffusion-controlled, and increasing the current density from 100 to 200 μA cm^{-2} doubles the rate of vacancy generation at the interface per time. For a given stripped capacity, this also halves the time available for vacancy removal from the interface and for redistribution by diffusion, including transport along the pore surface towards the pore edge. As a result, at high current densities, these transport processes are too slow to remove the same number of vacancies from the interface as at lower current densities. Therefore, vacancies are expected to accumulate over a larger fraction of the interface, which favors lateral pore expansion and the nucleation of additional pores rather than continued deepening of a smaller number of pores. Consequently, at higher current densities, diffusion limitation is expected to favor larger pore areas, compared to lower current densities. This increased pore area corresponds to a reduced remaining interfacial contact area, which enhances local stress concentrations and accelerates contact loss. As a result, despite the lower formed pore volume, higher current densities promote earlier failure.

This combined effect of diffusion-limited vacancy transport and stress-enhanced creep provides a consistent explanation for the experimentally observed reduction in pore volume at higher current densities in sodium. For potassium, however, the presence of bulk pores implies that the measured pore volume cannot be assigned exclusively to interfacial pores. Consequently, the reduced pore volume at 200 μA cm^{-2} cannot be unambiguously attributed to enhanced creep at the interface, limiting the direct applicability of the above interpretation to potassium.

This raises the question why bulk pore formation occurs in potassium, whereas no such behavior is observed for lithium and sodium under the investigated conditions. Such behavior is consistent with previous observations by Fischbach[15] for silver at temperatures of 800–900 °C (homologous temperature $T_H \approx 0.87–0.95$), where vacancy injection at the Ag|β-Al_2O_3 interface and subsequent vacancy transport into the silver bulk were demonstrated with bulk pore nucleation and growth as possible vacancy sinks. The homologous temperature of potassium at room temperature ($T_H \approx 0.89$) falls within this range and is significantly higher than that of sodium ($T_H \approx 0.80$) and lithium ($T_H \approx 0.66$). In combination with the higher self-diffusion coefficient of potassium ($D(K) = 1.9 \cdot 10^{-8}$ $cm^2 s^{-1}$) compared to sodium ($D(Na) = 5.8 \cdot 10^{-9}$ $cm^2 s^{-1}$) and lithium ($D(Li) = 5.2 \cdot 10^{-11}$ $cm^2 s^{-1}$) [66–68], we propose that bulk pore formation is driven by fast vacancy injection, vacancy diffusion and accumulation in the bulk. The influence of current density

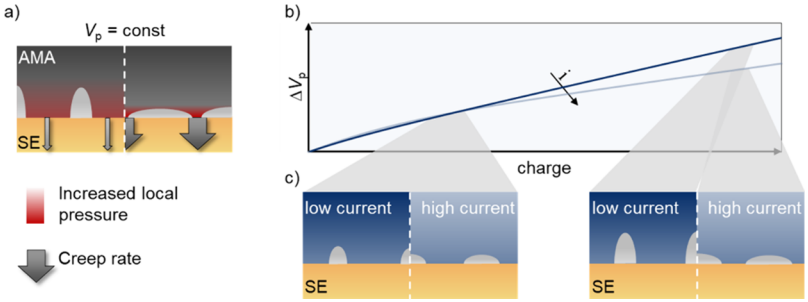


Figure 6. Schematic representation of the influence of pore geometry and current density on pore evolution: (a) Two pore geometries with identical pore volume. Flatter, laterally extended pores (right) lead to a smaller remaining interfacial contact area, resulting in higher local stress and enhanced creep compared to narrow, deep pores (left). (b) Evolution of pore volume for increasing current densities. (c) Higher current densities promote flatter, laterally extended pores. For clarity, a constant number of pores is assumed.

https://doi.org/10.1021/acselectrochem.6c00237
ACS Electrochem. 2026, 2, 2433–2449

Downloaded from pubs.acs.org/aecl/article-pdf/2/10/2433/6845074/2/ec-2026-00237p.pdf by KIT BIBLIOTHEK user on 02 November 2026

on bulk pore formation is likely governed by competing kinetic effects and cannot be resolved conclusively from the present data. An additional, more speculative mechanism for bulk pore formation is discussed in Supplementary Note 10. For higher capacities (> ~0.7 mAh cm^{-2}), the VIR shows a slight divergence between the two current densities before converging again starting from 2 mAh cm^{-2}, indicating differences in the apparent creep response. This suggests that bulk pores influence the creep response by redistributing the mechanical load.

Interfacial thermodynamics may further affect pore morphology. Formation of an interfacial pore replaces AMA|SE contact with free metal and SE surfaces. Therefore, weak adhesion or poor wetting lowers the energetic penalty for lateral opening along the interface and should favor flat, delamination-like pores, whereas strong adhesion should suppress interfacial dewetting. Interfacial bonding may additionally affect vacancy segregation between the interface and the metal bulk. For idealized interfaces, the vacancy segregation energy has been related to the work of adhesion and the metal surface energy, predicting that perfect wetting favors vacancy injection into the bulk metal and thereby suppresses interfacial void formation.[69] However, for incoherent interfaces, the average work of adhesion may not adequately describe vacancy redistribution because the vacancy energetics depend on the local bonding environment.[69] This is consistent with previous density functional theory (DFT) / kinetic Monte Carlo (KMC) simulations and operando SEM studies showing that lithiophilic interfaces can repel vacancies into the metal bulk and reduce void formation, while lithiophobic interfaces promote vacancy accumulation, void coalescence and contact loss.[64,70]

A quantitative comparison of the present interfaces is difficult because the reported adhesion values depend strongly on surface termination, passivation, surface roughness and contact morphology, including possible mechanical interlocking, as well as the calculation or measurement method (Supplementary Note 11).[69,71,72] Based on the evaluated literature data, Li|LLZO appears to be more lithiophilic than Na|NZSP is sodiophilic. Interfacial thermodynamics would therefore favor lateral pores in sodium and does not provide a consistent explanation for the deeper, more contact-preserving pore morphology observed for sodium. Thus, adhesion and wetting may contribute to pore morphology, but they do not appear to dominate the lithium–sodium difference under the present conditions.[69,71−74] The adhesion-based descriptor reflects the thermodynamic preference for interfacial separation under idealized equilibrium conditions. During stripping, pore evolution is a non-equilibrium process in which vacancies are continuously generated at the AMA|SE interface and must be removed by vacancy diffusion, adatom diffusion, or creep. The resulting pore morphology is therefore governed by the competition between interfacial thermodynamics, vacancy generation, transport kinetics, and stress-driven deformation.

For K|KBA, to the best of our knowledge, no room-temperature solid-state adhesion data are available. Therefore, we cautiously assume that interfacial thermodynamics is not a dominant descriptor of pore morphology in K|KBA either. Wetting experiments with liquid potassium on untreated KBA show a strong temperature dependence, ranging from non-wetting behavior at 100 °C to near-complete wetting at 240–250 °C (Supplementary Note 11).[75] Although these results are not directly transferable to the present conditions, this existing information about wetting does not provide evidence to support the idea that the formation of bulk pores in potassium is primarily driven by strong adhesion. Instead, pores are still expected to nucleate initially at the interface, while the later formation of bulk pores is consistently explained by the high homologous temperature, fast vacancy and atom transport, which allow vacancies to accumulate in the metal bulk.

Accordingly, pore formation in sodium and potassium can be described by the interplay of diffusion-limited vacancy transport and stress-driven creep, with bulk pore formation providing an additional contribution in potassium. In contrast, lithium exhibits a fundamentally different behavior, characterized by pronounced pore collapse and a strong current-density dependence. This raises the question why pore collapse occurs in lithium, whereas it is absent in sodium and potassium under the same conditions. The reason is that a very narrow parameter window regarding pressure, pore geometry and yield strength is required for collapse, which is only met for lithium in our case, as outlined in Supplementary Note 12.

While the regimes defined for lithium provide a useful reference, their direct transfer to sodium and potassium is limited. The current-density-independent regime at the onset of stripping (**Regime I**) is observed for all three alkali metals. However, due to the absence of pore collapse and constriction effects, no distinct **Regime II** can be identified for sodium and potassium. Instead, they exhibit a current density-dependent regime in which creep and diffusion processes act simultaneously, combining key characteristics of **Regime II** and **III** (see Supplementary Note 13 for details). Overall, the regimes can be assigned as follows: While lithium exhibits three distinct regimes of pore formation (**Regime I**: <0.6 mAh cm^{-2}; **Regime II**: 0.6–2 mAh cm^{-2}; **Regime III**: >2 mAh cm^{-2}), sodium and potassium show an extended current-density-independent **Regime I** up to ~2 mAh cm^{-2} (Na) and ~0.7 mAh cm^{-2} (K), followed by a current-density-dependent regime in which **Regime II** and **III** are superimposed due to the simultaneous action of creep and diffusion processes.

These differences in the sequence of pore formation steps indicate two distinct pore formation pathways (Figure 7). Both pathways begin with an identical initial stripping stage, during which vacancies are injected into the electrode and accumulate due to incomplete replenishment, resulting in pore nucleation. Subsequently, lateral pore expansion dominates, reducing the effective contact area while keeping the total pore volume for a given stripped charge independent of current density (**Regime I**).

For sodium and potassium, the evolution of local pressure during stripping promotes creep deformation (Figure 7a,b). In this case, enhanced creep and "long-range" adatom diffusion act simultaneously, thereby preventing excessive contact loss and promoting pore growth in depth. Deeper pores are only possible with sufficiently fast diffusion, consistent with the significantly higher vacancy diffusion rates of sodium and potassium compared to lithium. As a result, no measurable constriction effects are observed, and the stripping performance remains unlimited in the analyzed capacity range at the chosen current densities.

In contrast, lithium follows a different pathway (Figure 7b,c). After the initial lateral pore growth, increasing local pressure induces partial pore collapse, accompanied by continued lateral expansion and measurable constriction effects reflected in a rise

Downloaded from pubs.acs.org/aecic7/article-pdf/2/10/2433/6850742/ec-2026-00237p.pdf by KIT BIBLIOTHEK user on 02 November 2026

https://doi.org/10.1021/acselectrochem.6c00237
ACS Electrochem. 2026, 2, 2433−2449

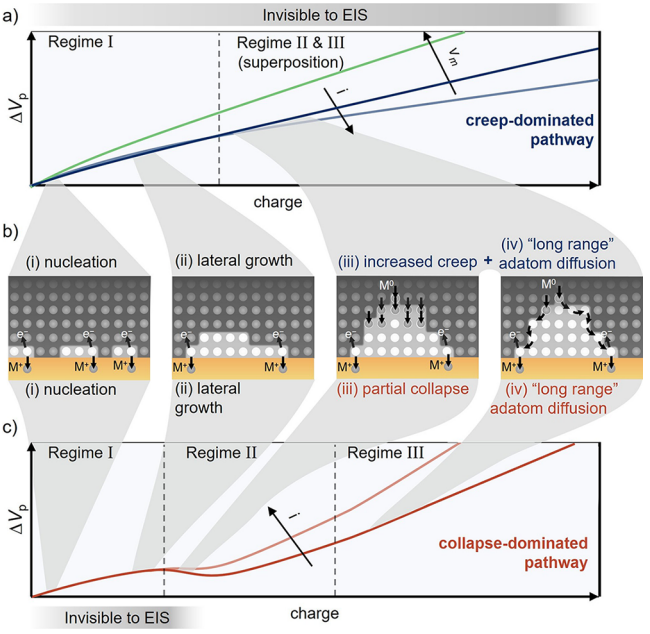


Figure 7. Pore formation mechanism for alkali metals. (a) Evolution of the pore volume for the pathway involving enhanced creep, valid for softer alkali metals with larger molar volumes (V_m) such as sodium and potassium. The blue curves denote the change in the pore volume (ΔV_p), appearing lighter for higher current densities, while the green color highlights the influence of increasing V_m. (b) Atomistic representation of the two pathways. (c) Evolution of the pore volume for the pathway involving partial pore collapse, valid for harder alkali metals with smaller V_m, such as lithium. The red curves represent the change in pore volume (ΔV_p); lighter colors correspond to higher current densities. Partially adapted from ref 43. Available under a CC-BY 4.0 license. Copyright 2025 Thomas A. Schall et al.

in interfacial resistance. Subsequently, the contact area stabilizes while lithium transport proceeds predominantly along pore surfaces via "long-range" adatom diffusion.

Although these two pathways differ in their dominant processes, they are governed by the same fundamental interplay of pore formation mechanisms. In the creep-dominated pathway observed for sodium and potassium, enhanced creep continuously reduces pore volume growth. In potassium, bulk pore formation additionally contributes to the measured total pore volume, such that the observed creep response cannot be attributed exclusively to the interface. In contrast, the collapse-dominated pathway observed for lithium is characterized by a short-term reduction in pore volume due to partial pore collapse. In both cases, pore evolution results from the interplay between (i) pore nucleation, (ii) lateral growth accompanied by contact area reduction, (iii) pore volume reduction through either increased creep or partial collapse, and (iv) pore deepening by "long-range" adatom diffusion. Considering the differences in yield strength and molar volume among the alkali metals, both pathways may occur in all systems under suitable combinations of current density, temperature, and pressure.

Material-Dependent Pore Evolution in Lithium, Sodium, and Potassium

Pore evolution substantially differs between lithium, sodium, and potassium, reflecting their distinct transport and mechanical properties. Figure 8 links the material-specific pore evolution to the mechanistic framework introduced above (Figure 7), with the processes (i–iv) assigned to the pore evolution. At the beginning of stripping, pores nucleate in all three alkali metals (Figure 8a). Subsequent pore growth diverges depending on the interplay of diffusion and mechanical properties. Lithium pores predominantly grow laterally, whereas sodium and potassium pores grow both laterally and in depth (Figure 8b). For sodium and potassium, the combination of faster diffusion and lower yield strength promotes transport- and creep-assisted stabilization of the remaining interfacial contact, thereby favoring pore growth in depth. In contrast, lithium pores remain comparatively flat, which is consistent with slower diffusion and higher yield strength. In the case of potassium, pores inside the metal must be considered. Bulk pore formation can be attributed to vacancy diffusion into the bulk followed by accumulation. The pores can approach their bulk equilibrium form due to rapid creep, high diffusivity, and high homologous temperature. It should be noted that the dilatometric pore volume data do not allow a direct distinction between interfacial and bulk pores. Since a sufficiently high vacancy concentration in the bulk is required, bulk pores are not expected to form at the initial stages and are therefore not shown in Figure 8 from the beginning.

As capacity increases, and because diffusivity and homologous temperature increase from sodium to potassium, pore growth in potassium becomes increasingly dominated by depth expansion. With increasing stripping capacity, the excess vacancy concentration in the bulk is expected to increase, thereby enhancing the probability of bulk pore formation within potassium. In contrast, sodium pores grow in both width and depth, while lithium pores mainly expand laterally (Figure 8c). As a result, lithium develops a large pore area with correspondingly small remaining contact areas between adjacent pores. Consequently, pores tend to coalesce, further reducing the contact area and increasing constriction effects, which cause the resistance increase. At the same capacity, the altered pore geometry triggers partial pore collapse (Figure 8d). No indication of contact area restoration is observed (see Supplementary Note 12 for details). In sodium, the growth of deeper pores dominates, maintaining a comparatively stable contact area, whereas in potassium, bulk pores continue to grow and form.

At later stages, the lithium interface stabilizes and pore growth transitions towards increased depth growth through "long range adatom diffusion" (Figure 8e). In sodium and potassium, pore growth predominantly continues in depth, with potassium additionally showing continued formation and growth of bulk pores (consistent with the preceding stage).

Overall, pore formation in alkali metals can thus be understood as the result of the interplay between vacancy transport, mechanical deformation, and pore geometry, determining whether a creep-dominated or a collapse-dominated pathway is followed.

Stress Analysis of Interfacial Pores

To further substantiate the proposed pore formation mechanism, in particular the role of stress-driven creep and its dependence on pore geometry, a combined analytical and numerical model analysis was performed. Using sodium as a representative system, the influence of pore geometry on the local stress distribution was investigated based on a model analysis of a single pore. Results for a single pore with different geometries are shown in Figure 9. The analysis of an isolated pore corresponds to the early stages of stripping, where pores are sufficiently separated (*i.e.*, by more than several pore diameters) and

Downloaded from pubs.acs.org/aecl/article-pdf/2/10/2433/6845074/2/ec-2026-00237p.pdf by KIT BIBLIOTHEK user on 02 November 2026

https://doi.org/10.1021/acselectrochem.6c00237
ACS Electrochem. 2026, 2, 2433−2449

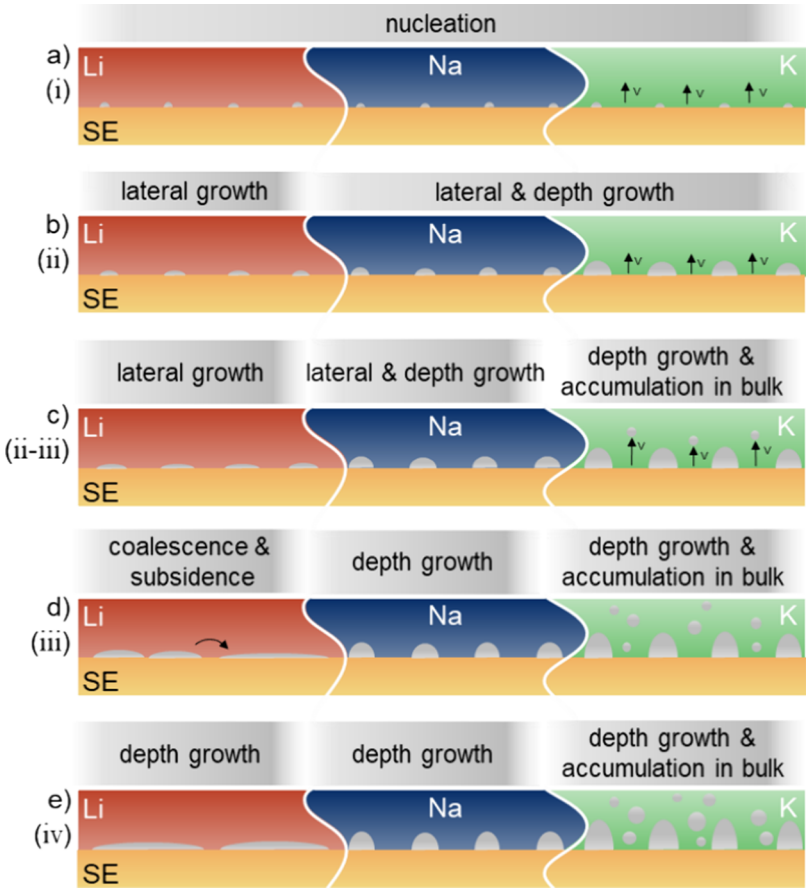


Figure 8. Material-dependent pore evolution during stripping in Li, Na, and K anodes. Pore nucleation and growth follow the mechanistic steps (i–iv) defined in Figure 7. Lithium tends to promote lateral pore growth, whereas sodium and potassium show combined lateral and depth growth. In potassium, vacancies accumulate in the metal at later stages and form bulk pores. Vacancy diffusion is shown only in the first potassium panels for clarity. (a) Interfacial pore nucleation in all three metals. (b) Lateral pore growth in lithium and combined lateral and depth growth in sodium and potassium. (c) Continued lateral growth in lithium, lateral and depth growth in sodium, and onset of bulk-pore formation in potassium. (d) Pore coalescence and subsidence in lithium, continued depth growth in sodium, and continued growth of interfacial and bulk pores in potassium. (e) Late-stage pore deepening in all three metals, with continued bulk-pore growth in potassium.

interactions between their stress fields are negligible. This assumption is consistent with the initial stages of the experiment, when solid-solid contact still covers most of the interface.

The FIB-SEM image (Figure 9a, left) shows pores at a sodium anode removed from the solid electrolyte. Under an applied far-field compressive stack pressure, the pore perturbs the local stress field, leading to stress amplification near the pore-metal-SE triple junction (pore edge), where the local stress σ_{zz} can significantly exceed the applied stress σ_{∞}.

This effect is particularly relevant for soft metals such as sodium, which exhibits a low yield strength (0.16–0.41 MPa).[46,47] Even modest stack pressures (~0.07 MPa) can therefore create local stress sufficient to activate inelastic deformation. Under sustained loading, this promotes creep-like deformation near the pore edge and contributes to pore growth reduction. This motivates a quantitative analysis of the stress concentration coefficient σ_{zz}^{max}/σ as a function of pore geometry. Here, σ_{zz}^{max} denotes the maximum normal stress perpendicular to the interface, located at the triple junction (Figure 9d, right).

To isolate shape effects, the interface is modeled as two semi-infinite elastic half-spaces (AMA above, SE below, axisymmetric) containing a half-elliptical pore characterized by its lateral half-length a and height b at the interface (Figure 9a, center). The aspect ratio (a/b) governs the pore geometry and strongly influences the magnitude of σ_{zz}^{max} and therefore the tendency for localized inelastic deformation (e.g., yielding or creep). In addition, the interfacial shear response affects the stress distribution. Two limiting cases are considered (Figure 9a, right):

- Frictionless contact interface (minimal shear transfer)
- Perfectly bonded interface (maximal constraint)

In the frictionless limit, analytical solutions show that σ_{zz}^{max} increases strongly with increasing aspect ratio (a/b), *i.e.*, flatter pores exhibit higher stress concentration. In contrast, the perfectly bonded case leads to stronger stress localization, and may give rise to a stress singularity at the pore edge due to elastic mismatch (see Supplementary Note 4 for details).

The frictionless contact model and perfectly bonded model should be interpreted as bounding cases rather than literal descriptions of the interface. A cohesive-zone model represents intermediate behavior, where finite shear strength limits stress

Downloaded from pubs.acs.org/aecic7/article-pdf/2/10/2433/6845074/2ec-2026-00237p.pdf by KIT BIBLIOTHEK user on 02 November 2026

https://doi.org/10.1021/acselectrochem.6c00237
ACS Electrochem. 2026, 2, 2433−2449

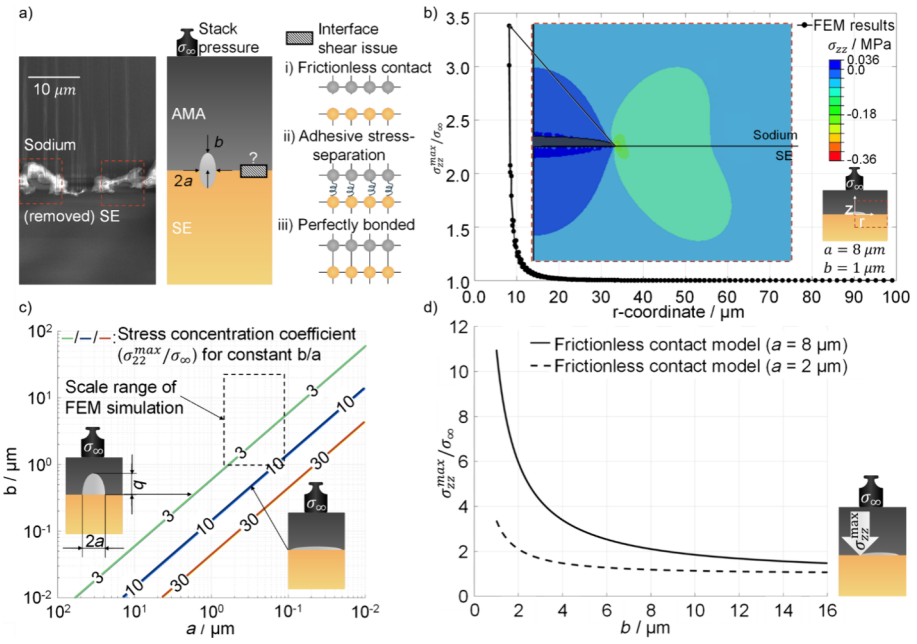


Figure 9. Effect of interfacial pore geometry on stress concentration at an AMA|SE interface. (a) FIB–SEM image of an interfacial pore at a peeled-off sodium anode after complete contact loss (4.2 mAh cm^{-2}, 200 μA cm^{-2}) and schematic of the electrode–SE stack subjected to compressive stack pressure (center). The pore is idealized as a half-elliptical cavity with half-length a along the interface and half-height b normal to the interface. To bound the role of interfacial shear transfer, two limiting interfacial conditions are considered (right): (i) Frictionless contact (free slip) and (iii) Perfectly bonded (no slip). A more realistic response is expected to lie between these bounds: (ii) adhesive stress separation with finite shear resistance. (b) Perfectly bonded interface (FEM): Predicted σ_{zz} stress field around a flat interfacial pore ($a = 8$ μm, $b = 1$ μm) under an applied far-field stack pressure of 0.07 MPa. The contour map and the corresponding σ_{zz} profile along the interface are shown. (c) Frictionless contact interface (analytical): Stress concentration coefficient σ_{zz}^{max}/σ from Neuber-type analytical solutions mapped as a function of a and b. Flatter pores (larger a/b) produce higher stress concentration. The black dashed box indicates the parameter range evaluated in (d). (d) Stress concentration coefficients from analytical shear-free predictions (solid and dashed lines for $a = 8$ μm, $a = 2$ μm, respectively).

transfer, resulting in an interfacial response between these two limits. The stress concentration is primarily governed by pore geometry. For experimentally relevant pore sizes, significant stress concentrations at the pore edge are expected.

Analytical solutions show that flatter pores generate stronger stress concentration at the pore edge. The interfacial condition then determines whether this concentration remains a smooth notch-like amplification or evolves into a mismatch-driven corner singularity (formally diverging at the edge; see Supplementary Note 4 and Figure S3). In the frictionless limit, the response is well described by the elastic pore/inclusion solution. In the perfectly bonded limit, the near-edge stress field is governed by an interface singularity arising from elastic mismatch, the severity of which depends on the Dundurs parameters (see Supplementary Note 4 for details). Despite this possible singularity, the stress distribution shown in Figure 9b remains meaningful. Only the local maximum at the pore edge cannot be assigned a well-defined finite value within this idealized limit. This is not critical for the present discussion, as the real interface is expected to be less constrained and therefore to exhibit a finite stress state below this upper bound. Accordingly, the analytical frictionless-contact solution shown in Figure 9d represents the lower limiting case. The actual interfacial stress distribution is expected to lie above this lower bound, showing that for experimentally relevant pore sizes high stress concentrations σ_{zz}^{max}/σ are expected at the edges, highlighting the strong influence of pore geometry (via a and b) on local stress amplification (see Supplementary Note 4 and Figure S3).

This analysis of a single pore shows that the stress at pore edges can readily reach local values that are sufficient to activate inelastic flow (*i.e.*, creep), which counteracts pore growth by accommodating vacancy injection. This geometric amplification is higher for flatter pores, supporting the hypothesis that growth of the pore volume is more strongly suppressed for flat pore geometries than for narrow, deep pores. As an isolated pore grows, the increasing pore size leads to enhanced stress concentration at the triple junction. This suggests that creep becomes relevant beyond a certain pore size, which may explain the initially elevated VIR at the onset of stripping and the similar pore volumes observed up to 2 mAh cm^{-2}, with deviations emerging only at higher capacities where the pores are larger. As the solid-solid contact area decreases, the distance between neighboring pores is reduced, leading to overlap and reinforcement of the stress fields (*i.e.*, σ_{zz}^{max} exceeds the single-pore case due to the overlap). The single-pore model is representative while pores remain sufficiently separated. At later stripping stages, with a lower remaining contact area and possibly high interfacial porosity, overlap and reinforcement of the stress fields of neighboring pores become increasingly important, and the single-pore model underestimates the local stress amplification. Consequently, the local stress concentration increases faster with increasing pore fraction at the interface, accelerating creep-driven deformation.

Downloaded from pubs.acs.org/aecic7/article-pdf/2/10/2433/6845074/2/ec-2026-00237p.pdf by KIT BIBLIOTHEK user on 02 November 2026

https://doi.org/10.1021/acselectrochem.6c00237
ACS Electrochem. 2026, 2, 2433−2449

These results highlight that pore geometry alone can induce significant stress amplification at the triple junction, promoting creep-driven metal transport that stabilizes the pore shape. In addition, materials with lower yield strength can accommodate plastic deformation at lower stresses, enabling continued pore deepening despite reduced stress concentrations. Thus, the trend of enhanced creep at low remaining contact areas associated with flat pore geometries is further amplified by stress concentrations at pore edges.

Toward Stable Stripping: Implications for Alkali Metal Anodes

The results consistently demonstrate that stripping stability is governed by the interplay between pore formation and mechanical response. In particular, the evolution of interfacial contact and pore morphology is strongly controlled by material properties such as yield strength and diffusion.

Lithium is prone to severe contact loss and resulting current constriction, which are critical for failure. In contrast, sodium and potassium exhibit more stable stripping, as their lower yield strength and higher creep rates promote geometries that better preserve interfacial contact. Potassium, however, shows a pronounced tendency toward internal pore formation. As these do not contribute to interfacial current constriction, they are likely less critical than interfacial pores. However, the implications of such pores remain unclear and may become critical under conditions of limited alkali-metal reservoirs.

These findings highlight yield strength as a central parameter of alkali-metal anodes that requires special attention. More generally, these results emphasize that pore geometry, rather than pore volume alone, governs interfacial stability. Lower yield strength facilitates creep-mediated stress relaxation and promotes more favorable pore geometries, thereby mitigating contact loss. At the same time, diffusion and interfacial properties must be balanced. High diffusivity improves vacancy removal from the interface and transport of alkali metal atoms through "long-range" adatom diffusion but may enable the formation of internal pores. In addition, molar volume plays a key role by governing the total pore volume and thus influencing pore growth. This introduces a potential trade-off between mechanical stability and energy density.

These insights support the hypothesis that reducing the local or effective yield strength of lithium, or otherwise facilitating easier plastic deformation, may shift its pore formation mechanism toward the more favorable pathway observed in sodium and potassium, *i.e.*, from collapse-dominated interfacial pore structures to geometries that better maintain interfacial contact. This interpretation is consistent with the lower pore formation for two-phase lithium–sodium anodes reported by Yoon et al.[76] Strategies such as alloying, microstructural engineering, or interface modification may enable targeted tuning of mechanical properties.

Our findings further suggest a pronounced path dependence, where the pore geometry established during the initial stages of stripping influences the subsequent evolution of the interface. This implies that the formation of deeper, less laterally extended pores may promote more stable stripping behavior and reduced contact loss at later stages, potentially motivating advanced current protocols based on pulsing and utilizing strategic current pauses.

For the three alkali metals under consideration, not all pore formation directly limits performance (in **Regime I** for lithium, and across the considered capacity range for sodium and potassium). This raises the question of whether pore formation must be considered detrimental in general, or whether non-critical pore geometries exist. This consideration applies only to pores that do not exhibit measurable current constriction.

CONCLUSIONS

Pore formation in sodium and potassium anodes is investigated experimentally and compared with that in lithium anodes at a low pressure of 0.07 MPa. We show that pore formation begins immediately upon stripping and is governed by a universal nucleation mechanism across all three alkali metals. At later stages, pore morphology and growth dynamics diverge depending on material properties such as yield strength, molar volume, and creep behavior. Sodium and potassium form deeper pores while maintaining a larger interfacial contact area, whereas lithium exhibits pronounced contact loss, pore collapse and coalescence, and constriction formation, ultimately limiting stripping performance.

Despite the different material properties and stripping pathways, all three systems follow the same fundamental mechanism involving pore nucleation, lateral pore growth, pore height reduction by increased creep or partial pore collapse, and "long-range" adatom diffusion. The pathways differ mainly in the temporal sequence of events: in lithium, pore collapse precedes "long-range" adatom diffusion, whereas in sodium and potassium, enhanced creep and "long-range" adatom diffusion occur simultaneously.

These results demonstrate that pore geometry governs interfacial stability. Lower yield strength promotes creep-mediated stress relaxation and enables pore geometries that better preserve interfacial contact, as observed for sodium and potassium. In contrast, lithium forms less favorable geometries due to its higher yield strength. Increasing the current density reduces the remaining contact area in all three alkali metals; however, due to enhanced creep, the formed pore volume is reduced for sodium and potassium, whereas lithium exhibits the opposite trend, with increasing pore volume at higher current densities. The interplay between yield strength, molar volume, and diffusion introduces a trade-off between interfacial stability and energy density.

These insights suggest that reducing the local or effective yield strength of lithium, or facilitating easier plastic deformation, may shift its pore formation behavior toward the more favorable pathway as observed in sodium and potassium. Together, these insights provide a basis for understanding pore evolution and for developing strategies to improve interfacial stability and performance in solid-state batteries. Further systematic studies on the influence of pressure and temperature on pore formation are required to clarify their influence on the pore formation mechanism and to assess the role of bulk pores, especially in potassium. Particular attention should be given to establishing whether pore formation can or must be completely suppressed depending on the application. Overall, pores form from the onset of stripping in the three tested alkali metals, but their impact on performance is governed by the resulting pore geometry and the associated evolution of interfacial contact.

ASSOCIATED CONTENT

Data Availability Statement

The data that support the findings of this study are available at JLUdata. https://doi.org/10.22029/jlupub-21088

Downloaded from pubs.acs.org/aecic7/article-pdf/2/10/2433/6845074/2/ec-2026-00237p.pdf by KIT BIBLIOTHEK user on 02 November 2026

https://doi.org/10.1021/acselectrochem.6c00237
ACS Electrochem. 2026, 2, 2433−2449

Supporting Information

The Supporting Information is available free of charge at https://pubs.acs.org/doi/10.1021/acselectrochem.6c00237.

Supplementary Notes 1–13 on experimental details, calculations, analyses of data reliability at high capacities, interfacial stress analyses, mechanistic considerations, adhesion and wetting, and literature comparisons; Figures S1–S15; Tables S1–S2 (PDF)

AUTHOR INFORMATION

Corresponding Authors

Thomas A. Schall – *Institute of Physical Chemistry and Center for Materials Research (ZfM), Justus-Liebig-University Giessen, Heinrich-Buff-Ring 17, D-35392 Giessen, Germany;* orcid.org/0009-0000-8717-1694; Email: thomas.schall@uni-giessen.de

Till Fuchs – *Institute of Experimental Physics I and Center for Materials Research (ZfM), Justus-Liebig-University Giessen, Heinrich-Buff-Ring 16, D-35392 Giessen, Germany;* orcid.org/0009-0007-2440-181X; Email: till.fuchs@uni-giessen.de

Jürgen Janek – *Institute of Physical Chemistry and Center for Materials Research (ZfM), Justus-Liebig-University Giessen, Heinrich-Buff-Ring 17, D-35392 Giessen, Germany;* orcid.org/0000-0002-9221-4756; Email: juergen.janek@uni-giessen.de

Authors

Maya Ziegler – *Institute of Physical Chemistry and Center for Materials Research (ZfM), Justus-Liebig-University Giessen, Heinrich-Buff-Ring 17, D-35392 Giessen, Germany*

Max Wacha – *Institute of Physical Chemistry and Center for Materials Research (ZfM), Justus-Liebig-University Giessen, Heinrich-Buff-Ring 17, D-35392 Giessen, Germany*

Qianli Ma – *Institute of Energy Materials and Devices, IMD-2: Materials Synthesis and Processing, Forschungszentrum Jülich GmbH, D-52425 Jülich, Germany;* orcid.org/0000-0002-4709-4927

Frank Tietz – *Institute of Energy Materials and Devices, IMD-2: Materials Synthesis and Processing, Forschungszentrum Jülich GmbH, D-52425 Jülich, Germany;* orcid.org/0000-0002-3724-7627

Janis K. Eckhardt – *Institute of Physical Chemistry and Center for Materials Research (ZfM), Justus-Liebig-University Giessen, Heinrich-Buff-Ring 17, D-35392 Giessen, Germany;* orcid.org/0000-0002-2799-0599

Chenjie Gan – *School of Engineering, Brown University, Providence, RI 02912, USA*

Aleksandar S. Mijailovic – *School of Engineering, Brown University, Providence, RI 02912, USA*

Brian W. Sheldon – *School of Engineering, Brown University, Providence, RI 02912, USA;* orcid.org/0000-0002-9593-891X

Complete contact information is available at: https://pubs.acs.org/doi/10.1021/acselectrochem.6c00237

Author Contributions

The experiments were designed and conducted by T.A.S. and M.Z. The cells were prepared by M.Z. and M.W., with Q.M. providing the NZSP solid electrolyte. T.A.S., J.K.E., T.F., and J.J. analyzed and interpreted the experimental data. C.G. conducted the FEM simulations and evaluated the simulative and analytical results. A.S.M. and B.W.S. supported the mechanical interpretation. The project was supervised by T.F. and J.J. The original draft was written by T.A.S. and then edited and supervised by F.T., J.K.E., A.S.M., B.W.S., T.F., and J.J.

Notes

During the preparation of this work, the authors used ChatGPT (by OpenAI), Copilot (Microsoft), Gemini (Google), and DeepL Write (DeepL) to improve readability and language. After using these tools, the authors reviewed and edited the content as needed and take full responsibility for the content of the publication.

The authors declare no competing financial interests.

ACKNOWLEDGMENTS

The authors would like to thank Prof. Kolling for valuable discussions and insightful advice. Special thanks are extended to Tim Klunz for the preparation of high-quality Li|LLZO|Li cells. Financial support from the Federal Ministry of Research, Technology and Space (BMFTR) within the projects KAFEBAR (03XP0565D), LiSI2 (03XP0509B), and SilKompAs (03XP0486D) is gratefully acknowledged. J.K.E. further acknowledges funding from the Hessian State Ministry of Higher Education, Research, and the Arts (HMWK). M.Z. and J.J. acknowledge funding by DFG (German Science Foundation) through the Cluster of Excellence POLiS (390874152). B.W.S., C.G., and A.S.M. acknowledge financial support from the NSF Grant DMR-2124775 and from the Assistant Secretary for Energy Efficiency and Renewable Energy, Office of Vehicle Technologies of the U.S. Department of Energy (DOE) through the Battery 500 Consortium. This work is part of a cooperative dissertation project between Justus Liebig University Giessen and Technische Hochschule Mittelhessen University of Applied Sciences at the Graduate Centre of Engineering Sciences at the Research Campus of Central Hessen.

REFERENCES

(1) Li, M.; Lu, J.; Chen, Z.; Amine, K. 30 Years of Lithium-Ion Batteries. *Adv. Mater.* **2018**, *30* (33), 1800561.

(2) Janek, J.; Zeier, W. G. A Solid Future for Battery Development. *Nat. Energy* **2016**, *1* (9), 16141.

(3) Randau, S.; Weber, D. A.; Kötz, O.; Koerver, R.; Braun, P.; Weber, A.; Ivers-Tiffée, E.; Adermann, T.; Kulisch, J.; Zeier, W. G.; Richter, F. H.; Janek, J. Benchmarking the Performance of All-Solid-State Lithium Batteries. *Nat. Energy* **2020**, *5* (3), 259–270.

(4) Zhang, Z.; Shao, Y.; Lotsch, B.; Hu, Y.-S.; Li, H.; Janek, J.; Nazar, L. F.; Nan, C.-W.; Maier, J.; Armand, M.; Chen, L. New Horizons for Inorganic Solid State Ion Conductors. *Energy Environ. Sci.* **2018**, *11* (8), 1945–1976.

(5) Krauskopf, T.; Richter, F. H.; Zeier, W. G.; Janek, J. Physicochemical Concepts of the Lithium Metal Anode in Solid-State Batteries. *Chem. Rev.* **2020**, *120* (15), 7745–7794.

(6) Gao, H.; Lin, C.; Liu, Y.; Shi, J.; Zhang, B.; Sun, Z.; Li, Z.; Wang, Y.; Yang, M.; Cheng, Y.; Wang, M.-S. Galvanostatic Cycling of a Micron-Sized Solid-State Battery: Visually Linking Void Evolution to Electrochemistry. *Sci. Adv.* **2025**, *11* (14), eadt4666.

(7) Wang, T.; Chen, B.; Liu, Y.; Song, Z.; Wang, Z.; Chen, Y.; Yu, Q.; Wen, J.; Dai, Y.; Kang, Q.; Pei, F.; Xu, R.; Luo, W.; Huang, Y.

Downloaded from pubs.acs.org/aecic7/article-pdf/2/10/2433/6845074/2/ec-2026-00237p.pdf by KIT BIBLIOTHEK user on 02 November 2026

Fatigue of Li Metal Anode in Solid-State Batteries. *Science* **2025**, *388* (6744), 311–316.
(8) Krauskopf, T.; Hartmann, H.; Zeier, W. G.; Janek, J. Toward a Fundamental Understanding of the Lithium Metal Anode in Solid-State Batteries—An Electrochemo-Mechanical Study on the Garnet-Type Solid Electrolyte $Li_{6.25}Al_{0.25}La_3Zr_2O_{12}$. *ACS Appl. Mater. Interfaces* **2019**, *11* (15), 14463–14477.
(9) Lu, Y.; Zhao, C.-Z.; Hu, J.-K.; Sun, S.; Yuan, H.; Fu, Z.-H.; Chen, X.; Huang, J.-Q.; Ouyang, M.; Zhang, Q. The Void Formation Behaviors in Working Solid-State Li Metal Batteries. *Sci. Adv.* **2022**, *8* (45), eadd0510.
(10) Majoni, S.; Janek, J. Investigation of Charge Transport across the Ag|AgI-interface: (II) Dilatometric Study of the Anodic Dissolution of Silver. *Berichte Bunsenges. Phys. Chem.* **1998**, *102* (5), 756–762.
(11) Meyer, M.; Rickert, H.; Schwaitzer, U. Investigations on the Kinetics of the Anodic Dissolution of Lithium at the Interface Li/Li3N. *Solid State Ion.* **1983**, *9–10*, 689–693.
(12) Vonalpen, U.; Bell, M. The Behaviour of the Lithium/Lithium-Nitride Interface under Anodic Polarisation. *Solid State Ion.* **1981**, *3–4*, 259–262.
(13) Kasemchainan, J.; Zekoll, S.; Spencer Jolly, D.; Ning, Z.; Hartley, G. O.; Marrow, J.; Bruce, P. G. Critical Stripping Current Leads to Dendrite Formation on Plating in Lithium Anode Solid Electrolyte Cells. *Nat. Mater.* **2019**, *18* (10), 1105–1111.
(14) Barai, P.; Fuchs, T.; Trevisanello, E.; Richter, F. H.; Janek, J.; Srinivasan, V. Study of Void Formation at the Lithium|Solid Electrolyte Interface. *Chem. Mater.* **2024**, *36* (5), 2245–2258.
(15) Fischbach, H. Leerstelleninjektion in Silber Während Elektrolytischen Abtrags Bei Hohen Temperaturen. *Int. J. Mater. Res.* **1980**, *71* (2), 115–119.
(16) Krauskopf, T.; Mogwitz, B.; Rosenbach, C.; Zeier, W. G.; Janek, J. Diffusion Limitation of Lithium Metal and Li–Mg Alloy Anodes on LLZO Type Solid Electrolytes as a Function of Temperature and Pressure. *Adv. Energy Mater.* **2019**, *9* (44), 1902568.
(17) Zhang, X.; Wang, Q. J.; Harrison, K. L.; Roberts, S. A.; Harris, S. J. Pressure-Driven Interface Evolution in Solid-State Lithium Metal Batteries. *Cell Rep. Phys. Sci.* **2020**, *1* (2), 100012.
(18) Koshikawa, H.; Matsuda, S.; Kamiya, K.; Miyayama, M.; Kubo, Y.; Uosaki, K.; Hashimoto, K.; Nakanishi, S. Dynamic Changes in Charge-Transfer Resistance at Li Metal/Li7La3Zr2O12 Interfaces during Electrochemical Li Dissolution/Deposition Cycles. *J. Power Sources* **2018**, *376*, 147–151.
(19) Yang, M.; Liu, Y.; Nolan, A. M.; Mo, Y. Interfacial Atomistic Mechanisms of Lithium Metal Stripping and Plating in Solid-State Batteries. *Adv. Mater.* **2021**, *33* (11), e2008081.
(20) Fuchs, T.; Ortmann, T.; Becker, J.; Haslam, C. G.; Ziegler, M.; Singh, V. K.; Rohnke, M.; Mogwitz, B.; Peppler, K.; Nazar, L. F.; Sakamoto, J.; Janek, J. Imaging the Microstructure of Lithium and Sodium Metal in Anode-Free Solid-State Batteries Using Electron Backscatter Diffraction. *Nat. Mater.* **2024**, *23* (12), 1678–1685.
(21) Zhang, X.; Osenberg, M.; Ziesche, R. F.; Yu, Z.; Kowal, J.; Dong, K.; Lu, Y.; Manke, I. Visualizing the Future: Recent Progress and Challenges on Advanced Imaging Characterization for All-Solid-State Batteries. *ACS Energy Lett.* **2025**, *10* (1), 496–525.
(22) Dixit, M. B.; Verma, A.; Zaman, W.; Zhong, X.; Kenesei, P.; Park, J. S.; Almer, J.; Mukherjee, P. P.; Hatzell, K. B. Synchrotron Imaging of Pore Formation in Li Metal Solid-State Batteries Aided by Machine Learning. *ACS Appl. Energy Mater.* **2020**, *3* (10), 9534–9542.
(23) Yonemoto, F.; Nishimura, A.; Motoyama, M.; Tsuchimine, N.; Kobayashi, S.; Iriyama, Y. Temperature Effects on Cycling Stability of Li Plating/Stripping on Ta-Doped Li7La3Zr2O12. *J. Power Sources* **2017**, *343*, 207–215.
(24) Sandoval, S. E.; Nelson, D. L.; Sridhara, H.; Thomas, T. A.; Lewis, J. A.; Cavallaro, K. A.; Shevchenko, P.; Dasgupta, N. P.; Usseglio-Viretta, F. L. E.; Finegan, D. P.; McDowell, M. T. Visualizing Diverse Lithium Growth and Stripping Behaviors in Anode-Free Solid-State Batteries with Operando X-Ray Tomography. *EES Batteries* **2025**, *1 (6)*, 1809–1821.
(25) Spencer Jolly, D.; Ning, Z.; Darnbrough, J. E.; Kasemchainan, J.; Hartley, G. O.; Adamson, P.; Armstrong, D. E. J.; Marrow, J.; Bruce, P. G. Sodium/Na β″Alumina Interface: Effect of Pressure on Voids. *ACS Appl. Mater. Interfaces* **2020**, *12* (1), 678–685.
(26) Eckhardt, J. K.; Klar, P. J.; Janek, J.; Heiliger, C. Interplay of Dynamic Constriction and Interface Morphology between Reversible Metal Anode and Solid Electrolyte in Solid State Batteries. *ACS Appl. Mater. Interfaces* **2022**, *14* (31), 35545–35554.
(27) Eckhardt, J. K.; Fuchs, T.; Burkhardt, S.; Klar, P. J.; Janek, J.; Heiliger, C. 3D Impedance Modeling of Metal Anodes in Solid-State Batteries–Incompatibility of Pore Formation and Constriction Effect in Physical-Based 1D Circuit Models. *ACS Appl. Mater. Interfaces* **2022**, *14* (37), 42757–42769.
(28) Eckhardt, J. K.; Fuchs, T.; Burkhardt, S.; Klar, P. J.; Janek, J.; Heiliger, C. Guidelines for Impedance Analysis of Parent Metal Anodes in Solid-State Batteries and the Role of Current Constriction at Interface Voids, Heterogeneities, and SEI. *Adv. Mater. Interfaces* **2023**, *10* (8), 2202354.
(29) Hunkel, M.; Surm, H.; Steinbacher, M. Dilatometry. Handbook of Thermal Analysis and Calorimetry. *Recent Adv. Tech. Appl.* **2018**, 103–129.
(30) Macherauch, E.; Zoch, H.-W. *Praktikum in Werkstoffkunde: 91 Ausführliche Versuche Aus Wichtigen Gebieten Der Werkstofftechnik*; Springer-Verlag, **2011**.
(31) Simmons, R. O.; Balluffi, R. W. Measurements of Equilibrium Vacancy Concentrations in Aluminum. *Phys. Rev.* **1960**, *117* (1), 52–61.
(32) Simmons, R. O.; Balluffi, R. W. Measurement of the Equilibrium Concentration of Lattice Vacancies in Silver near the Melting Point. *Phys. Rev.* **1960**, *119* (2), 600–605.
(33) Simmons, R. O.; Balluffi, R. W. Measurement of Equilibrium Concentrations of Lattice Vacancies in Gold. *Phys. Rev.* **1962**, *125* (3), 862–872.
(34) Simmons, R. O.; Balluffi, R. W. Measurement of Equilibrium Concentrations of Vacancies in Copper. *Phys. Rev.* **1963**, *129* (4), 1533–1544.
(35) Sprengel, W.; Würschum, R. High-Precision Dilatometry for the Study of Precipitation Processes and Microalloying Effects in Lightweight Alloys - A Specific Review. *Adv. Eng. Mater.* **2024**, *26* (19), 2400426.
(36) Michael, H.; Jervis, R.; Brett, D. J. L.; Shearing, P. R. Developments in Dilatometry for Characterisation of Electrochemical Devices. *Batter. Supercaps* **2021**, *4* (9), 1378–1396.
(37) Escher, I.; Hahn, M.; Ferrero, G. A.; Adelhelm, P. A Practical Guide for Using Electrochemical Dilatometry as Operando Tool in Battery and Supercapacitor Research. *Energy Technol.* **2022**, *10* (5), 2101120.
(38) Shin, R.-H.; Son, S. I.; Han, Y. S.; Kim, Y. D.; Kim, H.-T.; Ryu, S.-S.; Pan, W. Sintering Behavior of Garnet-Type $Li_7La_3Zr_2O_{12}$-Li_3BO_3 Composite Solid Electrolytes for All-Solid-State Lithium Batteries. *Solid State Ion.* **2017**, *301*, 10–14.
(39) Hupfer, T.; Bucharsky, E. C.; Schell, K. G.; Hoffmann, M. J. Influence of the Secondary Phase LiTiOPO4 on the Properties of $Li_{1+x}Al_xTi_{2-x}(PO_4)_3$ (x = 0; 0.3). *Solid State Ion.* **2017**, *302*, 49–53.
(40) Jonson, R. A.; McGinn, P. J. Tape Casting and Sintering of $Li_7La_3Zr_{1.75}Nb_{0.25}Al_{0.1}O_{12}$ with Li_3BO_3 Additions. *Solid State Ion.* **2018**, *323*, 49–55.
(41) Jin, Y.; McGinn, P. J. Al-Doped $Li_7La_3Zr_2O_{12}$ Synthesized by a Polymerized Complex Method. *J. Power Sources* **2011**, *196* (20), 8683–8687.
(42) Zhang, W.; Schröder, D.; Arlt, T.; Manke, I.; Koerver, R.; Pinedo, R.; Weber, D. A.; Sann, J.; Zeier, W. G.; Janek, J. (Electro)Chemical Expansion during Cycling: Monitoring the Pressure Changes in Operating Solid-State Lithium Batteries. *J. Mater. Chem. A* **2017**, *5* (20), 9929–9936.
(43) Schall, T. A.; Fuchs, T.; Eckhardt, J. K.; Klunz, T.; Mogwitz, B.; Sann, J.; Peppler, K.; Janek, J. Evolution of Pore Volume During

Downloaded from pubs.acs.org/aecic7/article-pdf/2/10/2433/6850742/ec-2026-00237p.pdf by KIT BIBLIOTHEK user on 02 November 2026

https://doi.org/10.1021/acselectrochem.6c00237
ACS Electrochem. 2026, 2, 2433–2449

Stripping of Lithium Metal in Solid-State Batteries Observed with Operando Dilatometry. *Small* **2025**, *21* (33), 2505053.
(44) Ma, Q.; Ortmann, T.; Yang, A.; Sebold, D.; Burkhardt, S.; Rohnke, M.; Tietz, F.; Fattakhova-Rohlfing, D.; Janek, J.; Guillon, O. Enhancing the Dendrite Tolerance of NaSICON Electrolytes by Suppressing Edge Growth of Na Electrode along Ceramic Surface. *Adv. Energy Mater.* **2022**, *12* (40), 2201680.
(45) Bay, M.; Wang, M.; Grissa, R.; Heinz, M. V. F.; Sakamoto, J.; Battaglia, C. Sodium Plating from Na-β″-Alumina Ceramics at Room Temperature, Paving the Way for Fast-Charging All-Solid-State Batteries. *Adv. Energy Mater.* **2020**, *10* (3), 1902899.
(46) Wang, M. J.; Chang, J.-Y.; Wolfenstine, J. B.; Sakamoto, J. Analysis of Elastic, Plastic, and Creep Properties of Sodium Metal and Implications for Solid-State Batteries. *Materialia* **2020**, *12*, 100792.
(47) Park, R. J.-Y.; Eschler, C. M.; Fincher, C. D.; Badel, A. F.; Guan, P.; Pharr, M.; Sheldon, B. W.; Carter, W. C.; Viswanathan, V.; Chiang, Y.-M. Semi-Solid Alkali Metal Electrodes Enabling High Critical Current Densities in Solid Electrolyte Batteries. *Nat. Energy* **2021**, *6* (3), 314–322.
(48) Spencer Jolly, D.; Perera, J.; Pu, S. D.; Melvin, D. L. R.; Adamson, P.; Bruce, P. G. High Critical Currents for Dendrite Penetration and Voiding in Potassium Metal Anode Solid-State Batteries. *J. Solid State Electrochem.* **2022**, *26* (9), 1961–1968.
(49) Wiberg, N. *Lehrbuch der Anorganischen Chemie*; De Gruyter, **2008**.
(50) Mineral Commodity Summaries 2025; U.S. Geological Survey, 2025.
(51) Hosaka, T.; Kubota, K.; Hameed, A. S.; Komaba, S. Research Development on K-Ion Batteries. *Chem. Rev.* **2020**, *120* (14), 6358–6466.
(52) El-Cell GmbH. *User Manual Dilatometer ECD-4-Nano: Release 1.4*, **2024**.
(53) El-Cell GmbH. *User Manual Dilatometer ECD-3-Nano: Release 1.1*, **2016**.
(54) White, G. K. Measurement of Thermal Expansion at Low Temperatures. *Cryogenics* **1961**, *1* (3), 151–158.
(55) Steinitz, M. O.; Genossar, J.; Schnepf, W.; Tindall, D. A. Simple, Versatile, and Compact Capacitance Dilatometer. *Rev. Sci. Instrum.* **1986**, *57* (2), 297–298.
(56) Carr, R. H.; McCammon, R. D.; White, G. K. The Thermal Expansion of Copper at Low Temperatures. *Proc. R. Soc. Lond. Ser. Math. Phys. Sci.* **1964**, *280* (1380), 72–84.
(57) Ma, Q.; Tsai, C.-L.; Wei, X.-K.; Heggen, M.; Tietz, F.; Irvine, J. T. S. Room Temperature Demonstration of a Sodium Superionic Conductor with Grain Conductivity in Excess of 0.01 S cm^{-1} and Its Primary Applications in Symmetric Battery Cells. *J. Mater. Chem. A* **2019**, *7* (13), 7766–7776.
(58) Ortmann, T.; Burkhardt, S.; Eckhardt, J. K.; Fuchs, T.; Ding, Z.; Sann, J.; Rohnke, M.; Ma, Q.; Tietz, F.; Fattakhova-Rohlfing, D.; Kübel, C.; Guillon, O.; Heiliger, C.; Janek, J. Kinetics and Pore Formation of the Sodium Metal Anode on NASICON-Type $Na_{3.4}Zr_2Si_{2.4}P_{0.6}O_{12}$ for Sodium Solid-State Batteries. *Adv. Energy Mater.* **2023**, *13* (5), 2202712.
(59) Neuber, H. *Kerbspannungslehre*; Springer Berlin Heidelberg: Berlin, Heidelberg, **1937**.
(60) Amstutz, H.; Vormwald, M. Elastic Prolate Spheroidal Inclusion in an Infinite Elastic Solid—an Exact Analysis of the Inclusion Stress by an Engineering Treatment of the Problem Based on the Corresponding Cavity Solutions. *Arch. Appl. Mech.* **2024**, *94* (6), 1503–1529.
(61) Institut für Arbeitsschutz der Deutschen Gesetzlichen Unfallversicherung (IFA). *Entry for Lithium in the GESTIS Substance Database (IFA)*, https://gestis.dguv.de/data?lang=en&name=008010.
(62) Institut für Arbeitsschutz der Deutschen Gesetzlichen Unfallversicherung (IFA). *Entry for Sodium in the GESTIS Substance Database (IFA)*, https://gestis.dguv.de/data?name=008080.
(63) Institut für Arbeitsschutz der Deutschen Gesetzlichen Unfallversicherung (IFA). *Entry for Potassium in the GESTIS Substance Database (IFA)*, https://gestis.dguv.de/data?lang=en&name=008150.
(64) Zhao, L.; Feng, M.; Wu, C.; Guo, L.; Chen, Z.; Risal, S.; Ai, Q.; Lou, J.; Fan, Z.; Qi, Y.; Yao, Y. Imaging the Evolution of Lithium-Solid Electrolyte Interface Using Operando Scanning Electron Microscopy. *Nat. Commun.* **2025**, *16* (1), 4283.
(65) Agier, J. A. B.; Shishvan, S. S.; Fleck, N. A.; Deshpande, V. S. Void Growth within Li Electrodes in Solid Electrolyte Cells. *Acta Mater.* **2022**, *240*, 118303.
(66) Mundy, J. N.; Barr, L. W.; Smith, F. A. Self-Diffusion in Potassium. *Philos. Mag.* **1967**, *15* (134), 411–413.
(67) Mundy, J. N.; Barr, L. W.; Smith, F. A. Sodium Self-Diffusion and the Isotope Effect. *Philos. Mag. J. Theor. Exp. Appl. Phys.* **1966**, *14* (130), 785–802.
(68) Lodding, A.; Mundy, J. N.; Ott, A. Isotope Inter-Diffusion and Self-Diffusion in Solid Lithium Metal. *Phys. Status Solidi B* **1970**, *38* (2), 559–569.
(69) Seymour, I. D.; Quérel, E.; Brugge, R. H.; Pesci, F. M.; Aguadero, A. Understanding and Engineering Interfacial Adhesion in Solid-State Batteries with Metallic Anodes. *ChemSusChem* **2023**, *16* (12), e202202215.
(70) Yang, C.-T.; Qi, Y. Maintaining a Flat Li Surface during the Li Stripping Process via Interface Design. *Chem. Mater.* **2021**, *33* (8), 2814–2823.
(71) Wang, M.; Sakamoto, J. Correlating the Interface Resistance and Surface Adhesion of the Li Metal-Solid Electrolyte Interface. *J. Power Sources* **2018**, *377*, 7–11.
(72) Gao, Z.; Yang, J.; Yuan, H.; Fu, H.; Li, Y.; Li, Y.; Ferber, T.; Guhl, C.; Sun, H.; Jaegermann, W.; Hausbrand, R.; Huang, Y. Stabilizing $Na_3Zr_2Si_2PO_{12}$/Na Interfacial Performance by Introducing a Clean and Na-Deficient Surface. *Chem. Mater.* **2020**, *32* (9), 3970–3979.
(73) Sharafi, A.; Kazyak, E.; Davis, A. L.; Yu, S.; Thompson, T.; Siegel, D. J.; Dasgupta, N. P.; Sakamoto, J. Surface Chemistry Mechanism of Ultra-Low Interfacial Resistance in the Solid-State Electrolyte $Li_7La_3Zr_2O_{12}$. *Chem. Mater.* **2017**, *29* (18), 7961–7968.
(74) Li, R.; Jiang, D.; Du, P.; Yuan, C.; Cui, X.; Tang, Q.; Zheng, J.; Li, Y.; Lu, K.; Ren, X.; Gao, S.; Zhan, X. Negating Na||$Na_3Zr_2Si_2PO_{12}$ Interfacial Resistance for Dendrite-Free and "Na-Less" Solid-State Batteries. *Chem. Sci.* **2022**, *13* (47), 14132–14140.
(75) Lu, X.; Bowden, M. E.; Sprenkle, V. L.; Liu, J. A Low Cost, High Energy Density, and Long Cycle Life Potassium–Sulfur Battery for Grid-Scale Energy Storage. *Adv. Mater.* **2015**, *27* (39), 5915–5922.
(76) Yoon, S. G.; Vishnugopi, B. S.; Nelson, D. L.; Yong, A. X. B.; Wang, Y.; Sandoval, S. E.; Thomas, T. A.; Cavallaro, K. A.; Shevchenko, P.; Alsaç, E. P.; Wang, C.; Singla, A.; Greer, J. R.; Ertekin, E.; Mukherjee, P. P.; McDowell, M. T. Interface Morphogenesis with a Deformable Secondary Phase in Solid-State Lithium Batteries. *Science* **2025**, *388* (6751), 1062–1068.

Downloaded from pubs.acs.org/aecic7/article-pdf/2/10/2433/6845074/2ec-2026-00237p.pdf by KIT BIBLIOTHEK user on 02 November 2026

https://doi.org/10.1021/acselectrochem.6c00237
ACS Electrochem. 2026, 2, 2433–2449